JGR Space Physics

RESEARCH ARTICLE
10.1029/2020JA027795

Special Section:
Results of the GEM Dayside Kinetics Southward IMF Challenge

Magnetopause Reconnection as Influenced by the Dipole Tilt Under Southward IMF Conditions: Hybrid Simulation and MMS Observation

Zhifang Guo[1], Yu Lin[1], Xueyi Wang[1], Sarah K. Vines[2], S. H. Lee[3], and Yuxi Chen[4]

[1]Physics Department, Auburn University, Auburn, AL, USA, [2]Johns Hopkins University Applied Physics Laboratory, Laurel, MD, USA, [3]CUA/NASA Goddard Space Flight Center, Greenbelt, MD, USA, [4]Department of Climate and Space Sciences and Engineering, University of Michigan, Ann Arbor, MI, USA

Key Points:
- Subsolar magnetopause X lines shift toward the Northern Hemisphere due to the effect of the negative tilted geomagnetic dipole angle
- The hybrid simulation magnetic fields and plasma date match MMS3 observations well during the magnetopause crossing
- Mirror mode waves appear in the middle of the magnetosheath downstream of the quasi-perpendicular shock

Correspondence to:
Z. Guo,
guozf@mail.iggcas.ac.cn

Citation:
Guo, Z., Lin, Y., Wang, X., Vines, S. K., Lee, S. H., & Chen, Y. (2020). Magnetopause reconnection as influenced by the dipole tilt under southward IMF conditions: Hybrid simulation and MMS observation. *Journal of Geophysical Research: Space Physics*, *125*, e2020JA027795. https://doi.org/10.1029/2020JA027795

Received 15 JAN 2020
Accepted 16 JUL 2020
Accepted article online 2 AUG 2020

Abstract Using a three-dimensional (3-D) global-scale hybrid code, the Magnetospheric Multiscale (MMS) reconnection event around 02:13 UT on 18 November 2015, highlighted in the Geospace Environment Modeling (GEM) Dayside Kinetic Challenge, is simulated, in which the interplanetary magnetic field (IMF) points southward and the geomagnetic field has a −27° dipole tilt angle. Strong southward plasma jets are found near the magnetopause as a result of the dayside reconnection. Our results indicate that the subsolar magnetopause reconnection X line shifts from the subsolar point toward the Northern Hemisphere due to the effect of the tilted geomagnetic dipole angle, consistent with the MMS observation. Subsequently, the reconnection X lines or sites and reconnection flux ropes above the equator propagate northward along the magnetopause. The formation and global distribution of the X lines and the structure of the magnetopause reconnection are investigated in detail with the simulation. Mirror mode waves are also found in the middle of the magnetosheath downstream of the quasi-perpendicular shock where the plasma properties are consistent with the mirror instability condition. As a special outcome of the GEM challenge event, the spatial and temporal variations in reconnection, the electromagnetic power spectra, and the associated D-shaped ion velocity distributions in the simulated reconnection event are compared with the MMS observation.

1. Introduction

Magnetic reconnection is a fundamental plasma process that occurs where magnetic topology of oppositely directed field lines rapidly changes, leading to abrupt acceleration and heating of plasmas (Dungey, 1961; Vasyliunas, 1975). This key process is not only considered to play an important role in producing solar flares (e.g., Masuda et al., 1994), coronal mass ejections (J. Lin & Forbes, 2000), and astrophysical plasma jets (Gosling et al., 2005) but also believed to be a principal mechanism for solar wind mass, momentum, and energy transfer into the Earth's magnetosphere (Birn et al., 2001; Dungey, 1961). In fact, the terrestrial magnetosphere provides a unique platform of collisionless space plasmas for understanding of the kinetic processes of magnetic reconnection.

As of now, reconnection has been observed in various boundary regions of the terrestrial magnetosphere. Under a southward interplanetary magnetic field (IMF), reconnection is observed to occur at the dayside magnetopause where the magnetic field inside the magnetopause points oppositely to that in the magnetosheath, forming magnetic flux ropes. These flux ropes may advect poleward and tailward with plasma flows. Under a strongly northward IMF, reconnection can take place at the high-latitude magnetopause poleward of the northern and southern cusps (Fuselier et al., 2012; Onsager et al., 2001). Reconnection has also been observed in the magnetotail plasma sheet, which causes large-scale changes of the magnetic field configuration and transient plasma dynamics, producing magnetospheric substorms and auroras (e.g., Angelopoulos et al., 2008; Nagai et al., 2001; Nakamura et al., 2006; Øieroset et al., 2001; R. Wang et al., 2016). Magnetic reconnection has also been found to take place in the magnetosheath (e.g., Guo et al., 2018; Pang et al., 2010; Phan et al., 2007, 2018; Retinò, Sundkvist, et al., 2007; Retinò, Vaivads, & Bale, 2007; Yordanova et al., 2016). On the whole, reconnection plays an important role in the solar wind-magnetosphere coupling. Reconnection events are generally divided into asymmetric reconnection, for example, at the magnetopause (Burch & Phan, 2016; Eastwood et al., 2013; Khotyaintsev et al., 2016;

Webster et al., 2018), where the magnetic field and plasma density are quite different across the current sheet, and symmetric reconnection, for example, in the magnetotail and magnetosheath (Gosling et al., 2005; Y. Lin & Lee, 1995; Phan et al., 2007, 2018). The structure of the reconnection site is strongly dependent on the plasma density and magnetic field on both sides of the current sheet. Our following research work is focused on the asymmetric reconnection at the magnetopause.

Generally, there are two scenarios for reconnection occurring at the dayside magnetopause: antiparallel reconnection and component reconnection. The former one preferentially occurs in regions where the terrestrial magnetic field and IMF are virtually pointing in opposite directions (e.g., Crooker, 1979; Luhmann et al., 1984). For a purely southward IMF, antiparallel reconnection is found to occur along the entire dayside magnetopause near the equatorial region (Trattner et al., 2007). In cases in which the IMF has a B_y component in addition to a southward component, the antiparallel reconnection region would be divided into two, located in the Northern and Southern Hemispheres (Trattner et al., 2004). Alternatively, component reconnection, in which a finite guide field exists, tends to occur in the region where the solar wind plasma first impinges upon the magnetopause. In any case, there is an X line along the magnetopause when the reconnection occurs (e.g., Fuselier et al., 2011; Gonzalez & Mozer, 1974; Moore et al., 2002; Sonnerup, 1974).

The reconnection sites or X lines are found to occur at different locations on the magnetopause under various IMF conditions. Based on 3-D plasma observations from the Toroidal Imaging Mass-Angle Spectrograph (TIMAS), Trattner et al. (2007) have predicted that X lines may extend along the ridge of the maximum magnetic shear between the magnetospheric and magnetosheath field lines on the magnetopause. These studies have proposed a model for a global continuous X line that turns out to extend in the equatorial plane when the IMF is purely southward (Trattner et al., 2007). During the period with a finite positive IMF B_y component, this X line may tilt relative to the equatorial plane, inclining toward north on the dawnside and south on the duskside of the dayside magnetopause. It leans in the opposite direction when the IMF has a finite negative B_y component (Trattner et al., 2012, 2018). Using magnetohydrodynamic (MHD) simulations, Komar et al. (2013) and Glocer et al. (2016) have investigated magnetopause reconnection X line location under various IMF conditions. Motion of the flux ropes has been investigated in other numerical simulations (Doss et al., 2015; Hoilijoki et al., 2017; Sibeck & Omidi, 2012; Sun et al., 2019).

Additionally, magnetopause reconnection can be modified significantly due to the variation of the Earth's dipole tilt angle. The dipole tilt is defined as the angle between the Earth's geomagnetic dipole pole and the geocentric pole (z axis in the geocentric solar magnetospheric [GSM] coordinate system). A change in the dipole tilt causes a significant change in the shape of the magnetopause (Boardsen et al., 2000; Y. Lin, Johnson, et al., 2010; R. L. Lin, Zhang, et al., 2010), which may change the distribution of X lines on the magnetopause. Using MHD simulations, Russell et al. (2003) and Park et al. (2006) indicate that the dayside magnetopause X lines shift away from the subsolar point during a purely southward IMF due to the effect of dipole tilt angle. Both global MHD simulations (Y. Liu et al., 2012; Lu et al., 2013; Park et al., 2006) and in situ observations (Hoilijoki et al., 2014) have shown that the shape of the magnetopause changes significantly with the geomagnetic dipole tilt angle. Using the data obtained by the Geotail and Magnetospheric Multiscale (MMS) mission spacecraft, Kitamura et al. (2016) have found that the dayside magnetopause reconnection line shifts toward the Northern Hemisphere under a largely tilted geomagnetic dipole and a southward IMF.

The kinetic physics of magnetopause reconnection has been investigated by various fully kinetic particle-in-cell (PIC) simulation models and hybrid kinetic models, in which ions are treated as particles while electrons are treated as a massless fluid. Using PIC (e.g., Cassak et al., 2017; Eastwood et al., 2013; Y.-H. Liu et al., 2015, 2018; Shay et al., 2016) and hybrid (Y. Lin & Xie, 1997; Xie & Lin, 2000) simulations, local structures and dynamics of magnetic reconnection at the dayside magnetopause within tens or hundreds of ion inertial lengths have been studied. On the global scale, however, the dayside reconnection regions are embedded in the curved magnetopause, whose geometry is determined by the interaction between the solar wind and the geomagnetic field. It is desirable to use a global-scale simulation model to investigate the global structure and consequence of magnetopause reconnection. Using a 3-D global-scale hybrid simulation model, Tan et al. (2011, 2012) have investigated multiple X line reconnection (MXR) and the cusp ion injections associated with the dayside magnetopause reconnection during southward IMF. Recently, the

generation of kinetic Alfvén waves (KAWs) in reconnection at the magnetopause was further studied by H. Wang et al. (2019) with this 3-D hybrid simulation model. The detailed structure of reconnection in the magnetopause obtained in the above global simulations, however, was not compared with space observations.

The purpose of this manuscript is to investigate the structure of magnetopause reconnection and compare our results from the 3-D global hybrid simulation with MMS observations, for a Geospace Environment Modeling (GEM) Dayside Kinetic Challenge event. This study focuses on the MMS observation event at 02:13 UT on 18 November 2015 analyzed by Kitamura et al. (2016). A goal of the GEM Dayside Kinetic Challenge is to understand the kinetic processes of magnetopause reconnection through comparisons between observations and numerical models. To this end, a common set of IMF and solar wind conditions are used for various MHD and kinetic models, in which the solar wind plasma conditions are the same as those observed by the Wind spacecraft in the solar wind but the IMF conditions are simplified as being purely southward (https://ccmc.gsfc.nasa.gov/support/GEM/Dayside_Kinetic_Processes/Dayside_Kinetic_Challenge/Introduction.php). Our 3-D global hybrid model, which solves the fully kinetic ion physics, is used to investigate this dayside magnetopause reconnection event in the presence of a largely tilted geomagnetic dipole. The spatial structure, electromagnetic wave power spectrum, and the ion velocity distributions in the simulated reconnection event are compared with the MMS observations. In addition, the formation and evolution of the magnetopause subsolar X lines, the effects of the dipole tilt angle on the X line location, the detailed structure of the ion diffusion region, and mirror mode waves in the magnetosheath are presented, which have not be investigated in the previous global hybrid simulations.

The layout of this paper is as follows: In section 2, we briefly introduce the simulation model and MMS-3 data set. In section 3, simulation results and observations are presented and compared, and the summary and discussion are given in section 4.

2. Simulation Model and Observational Data

In this study, we use a 3-D dayside global-scale hybrid simulation model (Guo et al., 2018; Y. Lin & Wang, 2005; Tan et al., 2011) to investigate the GEM Dayside Kinetic Challenge magnetopause reconnection event observed by MMS under southward IMF. The parameters chosen in the simulation run are listed at the Community Coordinated Modeling Center (CCMC, https://ccmc.gsfc.nasa.gov/support/GEM/Dayside_Kinetic_Processes/Dayside_Kinetic_Challenge/Introduction.php). Initially, the Earth's magnetic dipole axis is tilted tailward by 27°, and the IMF is purely southward with a magnitude of 6 nT. The solar wind mass density in the solar wind used in the simulation is 9.5 amu/cm^3. The solar wind, carrying the ion and electron fluid, flows toward the Earth's dipole field along the x direction with a speed of 360 km/s, corresponding to the Alfvén Mach number of $M_A \approx 8.5$.

In the present simulation, the Alfvén Mach number, magnetic field, and ion density all have realistic values, but the ion inertial length is larger than the realistic value due to the limit of computational resources. The solar wind ion inertial length, $d_{i_0} = c/\omega_{pi0}$, is chosen to be 0.1 R_E in our simulation. Spherical coordinates are adopted in the simulation model, with a grid number of $n_r \times n_\theta \times n_\phi = 220 \times 114 \times 150$ for the run. In this coordinate system, the zenith angle θ is measured from the positive GSM z axis, and the azimuthal angle φ is measured from the negative GSM y axis. Nonuniform grids are used in the radial (r) direction to produce a higher resolution with grid spacing $\Delta r = 0.05\ R_E$ near the magnetopause. The hybrid model is valid for low-frequency physics with $k\rho_i \sim 1$ (wavelength $\lambda \sim 6\rho_i$), where k is the wave number and ρ_i is the ion Larmor radius. For this range of wave wavelength, the ion kinetic physics at the magnetopause and in the magnetosheath are resolved with grid sizes ~ρ_i or ion inertial length d_i. Given that the ion number density in the magnetosheath and around the magnetopause is on the order of $N \approx 4N_0$ and $d_i = \sqrt{\frac{N_0}{N}}\, d_{i0}$, where N_0 is the number density of the solar wind, the ion inertial length is around $d_i = 0.05\ R_E$. Therefore, the grid size $\Delta r = 0.05\ R_E$ used is small enough to resolve the ion kinetic physics. A small current-dependent collision frequency, $\upsilon = 0.02\Omega_i J/J_0$, is imposed to simulate the ad hoc anomalous resistivity and in order to trigger magnetic reconnection in the simulation, where J is the current density, Ω_i is local ion gyrofrequency, $J_0 = B_0/\mu_0\, d_{i0}$, and B_0 is the IMF strength.

In our simulation, the typical time step interval for ion particle motion is $\Delta t = 0.05\Omega_{i0}^{-1}$, where the Ω_{i0} is the solar wind ion gyrofrequency, in order to resolve the finite ion gyroradius effects. Meanwhile, subcycling to the particle push is used for the update of the magnetic field. In the dipole field region near the Earth, the fast mode speed is large. This necessitates the use of a field time step (δt) much smaller than the particle steps in order to satisfy the Courant condition associated with the fast mode. In our simulation, 20 time steps ($\delta t = 0.0025\Omega_{i0}^{-1}$) were used to update the fields for each particle time step.

The magnetosphere, magnetopause, magnetosheath, and bow shock form self-consistently as the inflowing solar wind interacts with the dipole field, where the dipole field strength at the Earth's equatorial surface is $5{,}200B_0$, which is 31,200 nT. In this simulation, the magnetic field B and ion number density N are scaled by the solar wind IMF B_0 and ion density N_0, respectively. The time t is expressed by the inverse of the solar wind ion gyrofrequency Ω_{i0}^{-1} (where $\Omega_{i0} = eB_0/m_i$), and ion flow velocity V is normalized by the Alfvén speed V_{A0} (where $V_{A0} = B_0/\sqrt{\mu_0 m_i N_0}$) in the solar wind. Hence, the electric field is scaled by $V_{A0}B_0$. When comparing the simulation results with observation, real units are used.

When compared with the observation, a scaling factor needs to be considered for time t in the simulation. For this case with a solar wind mass density of 9.5 amu/cm^3, the realistic value of the solar wind ion inertial length is 0.0122 R_E, a factor of 8.2 smaller than the value of d_{i_0} (0.1 R_E) used in the simulation. The solar wind Alfvén speed $V_{A0} = d_{i0}\Omega_{i0}$, where Ω_{i0} is the (realistic) value of the solar wind ion gyrofrequency, used in the simulation is thus a factor of 8.2 faster than that in reality, while the sizes of the bow shock and the magnetopause in unit of R_E are realistic. The global convection time, therefore, is a factor of 8.2 shorter than the realistic value. To scale back based on the realistic convection time, we increase the time by a factor of 8.2 in order to make a comparison between the observation and the simulation.

In our self-consistent scheme, the ions are accelerated by the electric and magnetic field, while the electric field satisfies the generalized Ohm's law combined with Ampere's law, and the magnetic field is advanced with Faraday's law. In order to illustrate the simulation results on the spatial scales of the magnetosphere, the length is plotted in units of the Earth radius (R_E), and GSM coordinates are used, in which x points to the Sun and z points north. The y axis points from dawn to dusk. With the Earth located at the origin $(x, y, z) = (0,0,0)$ R_E, the simulation system contains a domain with GSM $x > 0$ with the range of $3.5R_E \le r \le 25R_E$. Solar wind boundary conditions with a constant inflow plasma and IMF B_0 are used at $r = 25$ R_E. At this boundary, the magetic field is simply the constant IMF. The electric field corresponds to $-V_{i0} \times B_0$, where V_{i0} is the ion bulk flow of the solar wind. The outflow boundaries are used at the boundaries near $x = 0$. At these boundaries, the electric field and the tangential components of the magnetic field are free, that is, with their first derivatives along the boundary normal being 0. The value of the normal component of the magnetic field is determined by the condition of $\nabla \cdot B = 0$. Since the plasma flows are predominantly super-Alfvénic outflows at these boundaries, any particles crossing these boundaries are simply removed from the simulation domain. The inner boundary, at $r = 3.5$ R_E, is assumed to be an ideal conducting, where the tangential component of the electric field are assumed to be 0, and the normal component of the magnetic field is held at the initial value. The small number of particles that can reach the boundary is simply reflected.

For the region of the inner magnetosphere, a cold, incompressible ion fluid is assumed to be dominant at $r < 6.5$ R_E, while our simulation focuses on the dynamics and ion kinetic physics in the outer magnetosphere. Since the plasma in the inner magnetosphere is dense, the use of the fluid approximation, instead of following individual particles in the strong magnetic field, results in the saving of enormous computational resources. Our code allows the particles and fluid to occupy the same spatial volume. This is necessary because there will be energetic particles entering regions near the Earth along the high-latitude field lines. The number density of the cold ion fluid is assumed to be

$$N_f = \left(N_{eq}/(r/1R_E)^3\right)[1 - \tanh(r/1R_E - 6.5)],$$

where $N_{\mathrm{eq}} = 1{,}000N_0$ is the ion fluid density at $r = 1$ R_E. The detailed descriptions can be referred to Lin et al. (2014) and Swift (1996).

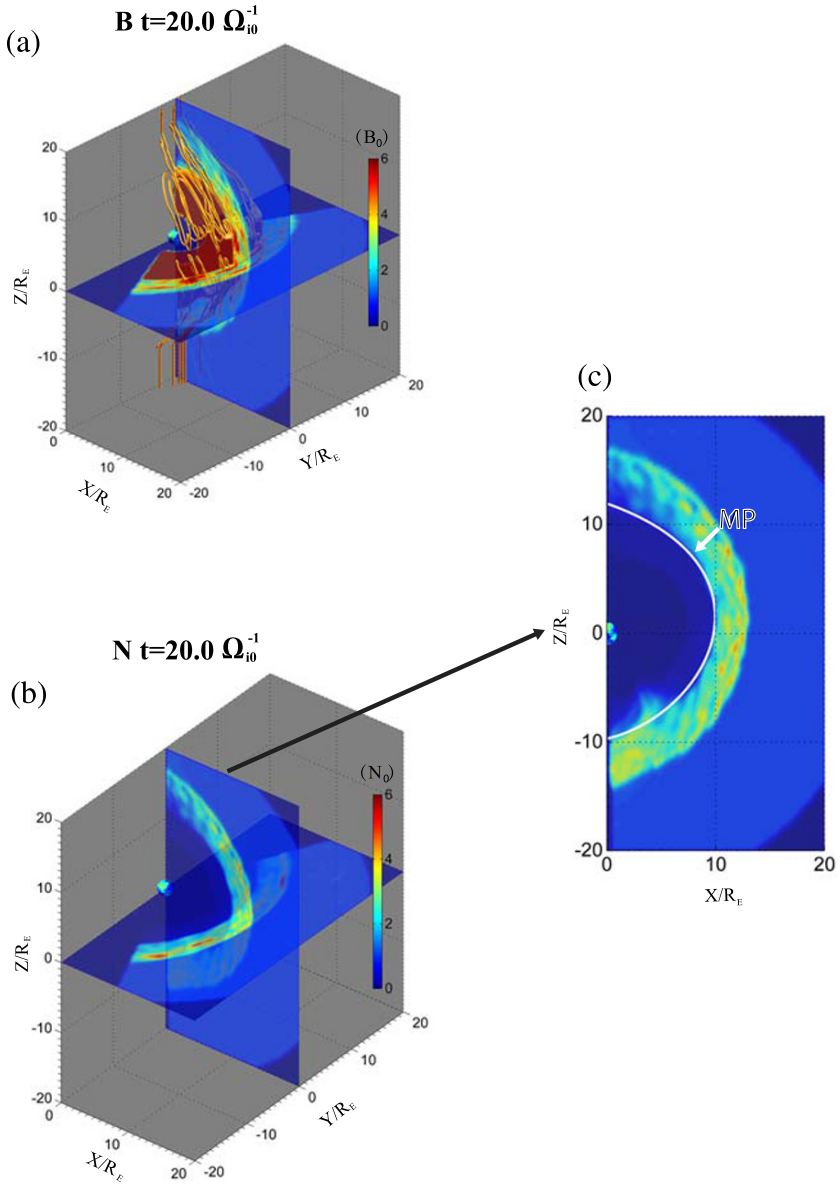

Figure 1. Contours of (a) the magnetic field strength B and (b) ion density N in the noon meridian and equatorial planes and (c) ion density N in the meridian plane, at $t = 20.0\Omega_{i0}^{-1}$. The orange lines are reconnected field lines at the magnetopause. The white curve in (c) marks the magnetopause position.

Observations used for comparisons with the simulation are from the MMS spacecraft when the spacecraft traversed the magnetopause near the subsolar point at (9.7, −1.0, −0.3) R_E in the GSM coordinate system around 02:13 UT on 18 November 2015. MMS is composed of four identical spacecraft flying in a closely spaced tetrahedral configuration (Burch, Moore, et al., 2016). Because the average separation of the four MMS spacecraft was ~10 km on 18 November 2015, data shown here are only from MMS-3. The MMS time series data are displayed using the Space Physics Environment Data Analysis System (SPEDAS) routines (Angelopoulos et al., 2019). Magnetic field data are from the Fluxgate Magnetometer (FGM) (Russell et al., 2016). The low-energy ion data (energies of ~10 eV to 27 keV) are from the Fast Plasma Investigation (FPI)-Dual Ion Spectrometer (FPI-DIS), which measures the full three-dimensional ion distribution and provides low-energy ion density, temperatures, and velocity (Pollock et al., 2016). Over the magnetopause crossing interval of 02:10 through 02:16 UT, FGM "fast survey" mode data, with a cadence of 16 vectors/s, are used. High time resolution "burst" data, with a sampling rate of 150 ms for FPI-DIS, are used

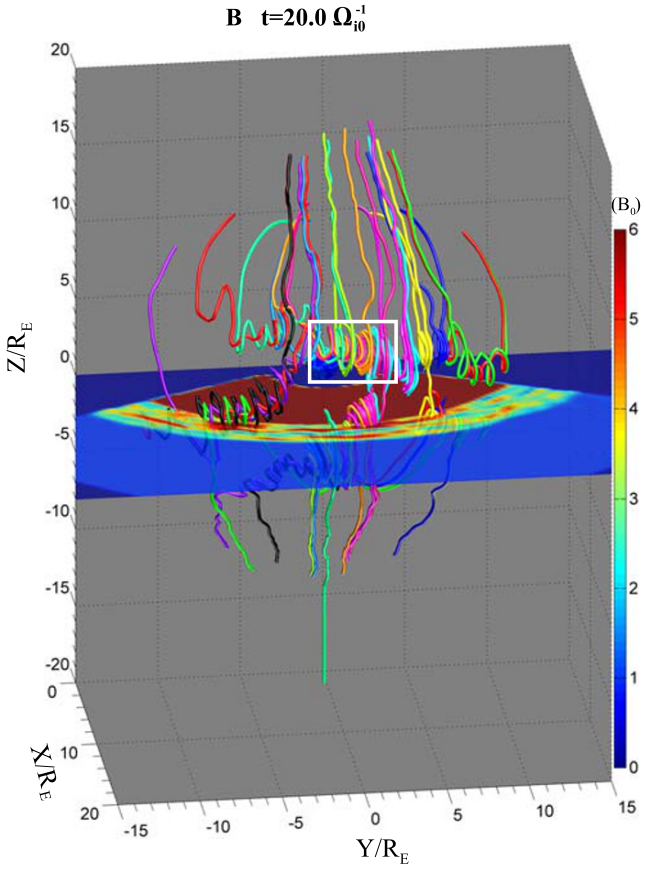

Figure 2. Magnetic field line configuration in the 3-D global view near the magnetopause at $t = 20.0\Omega_{i0}^{-1}$. Lines of different colors are reconnected field lines (flux ropes) at the magnetopause. The contours in the equatorial plane show the magnetic field strength B.

when available for the ion observations. For this magnetopause crossing, the burst data were available from 02:08:54–02:15:04 UT. Fast survey mode data from FPI-DIS, with a time cadence of 4.5 s, are used from 02:15:04–02:16:00 UT and combined with the burst ion data to cover the full magnetopause crossing interval. The magnetic field and ion velocity are rotated from GSM coordinates into a boundary normal (LMN) coordinate system using the LMN unit vectors from Kitamura et al. (2016), with L = (0.1974, 0.2013, 0.9594) GSM, M = (−0.1170, −0.9669, 0.2269) GSM, and N = (0.9733, −0.1570, −0.1673) GSM. This LMN coordinate system was derived from a combination of the minimum variance of the current density and the maximum variance of the magnetic field over the interval of 02:12:05 to 02:13:20 UT (see Kitamura et al., 2016, for more details). Magnetic field power spectral densities (PSDs) are generated from fast Fourier transforms (FFTs) of the fast survey FGM data. The magnetic field is first filtered via a band-pass filter of 0.005–8 Hz (i.e., up to the Nyquist frequency) and then rotated into a magnetic field aligned coordinate system, where $\perp x = x = y \times z$, $\perp y = y = z \times$ XGSE, and $|| = z = B/|B|$. The FFTs are taken over time intervals representative of the outer magnetosphere (01:30–01:51 UT), magnetopause current layer (02:10–02:15 UT), and magnetosheath (02:15–02:55 UT).

3. Simulation and Observational Results

3.1. Overall Simulation Results

As described in section 2, in our 3-D global hybrid simulation, we use the parameters listed at the CCMC (https://ccmc.gsfc.nasa.gov/support/GEM/Dayside_Kinetic_Processes/Dayside_Kinetic_Challenge/Introduction.php), including a southward IMF and a largely tilted geomagnetic dipole. Initially, the Earth's dipole magnetic field is imposed in $r \leq 10\ R_E$ with a −27° dipole tilt angle, which then interacts with the uniform solar wind and IMF in $r > 10\ R_E$. The bow shock, magnetosheath, and magnetopause are formed in a self-consistent manner at $t = 6.0\Omega_{i0}^{-1}$. Magnetic reconnection is initiated around $z \sim 0.6\ R_E$ at $t \approx 8.0\Omega_{i0}^{-1}$, near the locations where the magnetic field is antiparallel across the initial-stage magnetopause. As the solar wind continuously interacts with the subsolar magnetopause, the subsolar reconnection X line is settled further northward, oscillating around $z \sim 1.8\ R_E$ in the noon meridian plane at $t \geq 20.0\Omega_{i0}^{-1}$.

To illustrate the overall position of the dayside magnetopause, Figures 1a and 1b depict the magnetic field strength and ion density, respectively, in the noon meridian and equatorial planes at $t = 20.0\Omega_{i0}^{-1}$, together with same typical magnetic flux ropes shown by orange lines. The color contours of the ion density in the meridian plane are highlighted in Figure 1c. The central position of the magnetopause, which is indicated by the white curved curve in Figure 1c, can be identified by the sharp gradients of the magnetic field strength and ion density around $x = 9.83\ R_E$ through the subsolar point. The flux ropes (FTEs) are formed due to the magnetopause MXR.

Figure 2 highlights the structure of the magnetic flux ropes at the magnetopause in a 3-D global view at $t = 20.0\Omega_{i0}^{-1}$. The contours in the equatorial plane show the magnetic field strength. In this figure, lines of different colors indicate different reconnection field lines (flux ropes) at the magnetopause, and these field lines connect between IMF and the Earth's dipole field (to the North and South Poles). The magnetopause flux ropes extend in the y direction along the dayside magnetopause with helical magnetic field line structures, as also shown in Tan et al. (2011). The flux ropes around the subsolar region are centered at $z \sim 4.5\ R_E$ above the equator, as denoted by the white rectangle in Figure 2. The topology of field lines at the magnetopause indicates that there is a reconnection X line above the equator.

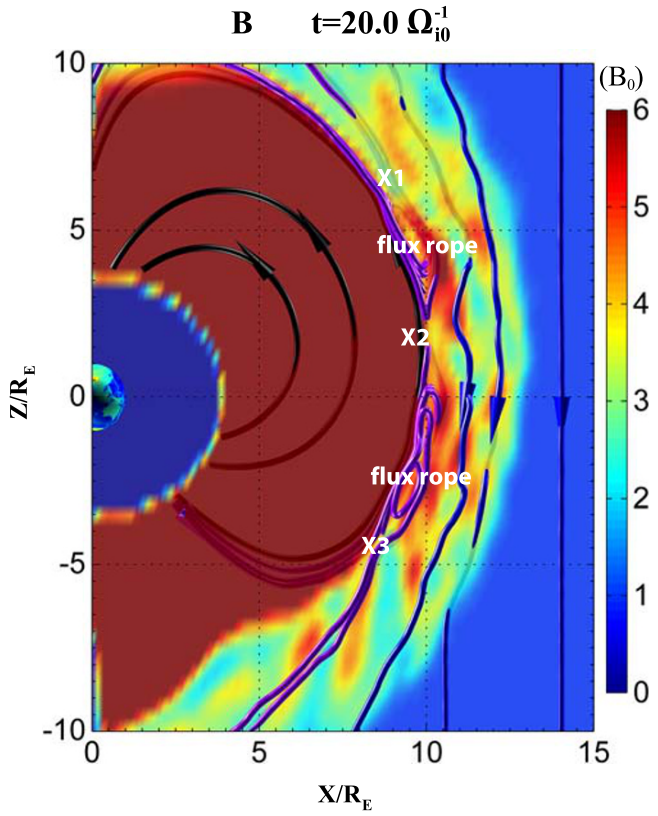

Figure 3. Contours of the magnetic field strength in the noon meridian plane at $t = 20.0\Omega_{i0}^{-1}$. The closed dipole field lines are in black. The violet field lines are the reconnected field lines at the magnetopause. Field lines in blue are open field lines in the magnetosheath and solar wind. The arrows display the magnetic field direction.

In our simulation, an X point of the X lines can be identified by the magnetic field configuration and characteristics of particle acceleration. Near the X point, the magnetic field lines must have an X type configuration. This X type configuration is determined by mapping the 3-D field lines onto a local xz reference plane. According to the magnetic field directions around the X point, four types of field lines are identified near an X point: dipole field lines on the earthward side of the magnetopause current sheet, magnetosheath field lines on the sunward of the current sheet, open field lines threading from the magnetosheath side to the magnetospheric side, and those connecting from the magnetospheric side to the magnetosheath side. In the vicinity of the X point, Hall quadrupolar perturbations in δB_y are present, with a larger δB_y on the magnetosheath side of the reconnection region than on the magnetospheric side. Such asymmetric quadrupolar structure will be further elaborated in Figure 6. In addition, two opposite ion flow jets, pointing away from the X point, can be found in the outflow regions on the two sides of the reconnection site. More details of the flow jets will also be given in Figures 6 and 7. Finally, by connecting the X points in a series of such xz planes (e.g., with an increment of $\delta y = 0.2\ R_E$), an X line segment naturally forms. The details of this method can be referred to Tan et al. (2011). A similar method of identifying the X line by the magnetic field configuration and the structure of flow jets has also been used by Y.-H. Liu et al. (2015, 2018).

To illustrate the X line locations at the magnetopause, Figure 3 shows a close-up of the magnetic field around the noon-meridian plane at $t = 20.0\ \Omega_{i0}^{-1}$ obtained in our simulation. Three colors of the magnetic field lines are shown in this figure, with the black ones being the closed dipole field lines, the violet field lines marking the reconnected field lines (flux ropes) at the magnetopause, and the blue ones representing the open field lines in the magnetosheath and solar wind. The arrows in Figure 3 display the directions of the local magnetic field. The colored sphere at the origin represents the Earth. Two looped flux ropes are formed between two neighboring X lines corresponding to MXR (Fu & Lee, 1985) shown by the violet field lines. Three reconnection X points shown by white labels "X1," "X2," and "X3" are found at the magnetopause, in which "X2" denotes the magnetopause reconnection point near the subsolar region. It is found that, compared with the cases without a dipole tilt, in which the magnetopause reconnection is found near the equatorial region (e.g., Dungey, 1961; Park et al., 2006), the subsolar X lines in our case are shifted toward the Northern Hemisphere due to the changes in the global geometries of the reconnected magnetic fields between the magnetosphere and the magnetosheath. As to be further elaborated below, the magnetopause reconnection site at the subsolar region is above the equatorial plane, due to the existence of the tailward dipole tilt angle.

To understand the effects of the dipole tilt angle on the magnetopause reconnection X point around the subsolar region, we have run cases with various dipole tilt angles. Figures 4a–4d show the magnetic field line configuration at the magnetopause around the noon meridian plane for cases in which the Earth's dipole tilt angle is equal to (a) 0°, (b) −15°, (c) −27° (the present case), and (d) 15°. The red arrow in each plot indicates the direction of the dipole moment. Three colors of the magnetic field lines are shown, with the black ones being the closed dipole field lines, the violet field lines marking the reconnected field lines (flux ropes) at the magnetopause, and the blue ones representing the open field lines of the magnetosheath. The magnetopause reconnection X line is found at the subsolar equator ($z \approx 0\ R_E$) in Case (a), as shown in Figure 4a. There is a reconnection X line at $z \approx 1.1\ R_E$, slightly shifted northward in Case (b) with a slightly tailward dipole tilt, as shown in Figure 4b. In the present case for the GEM dayside challenge event, in which the Earth's dipole axis is tilted tailward by 27°, a reconnection X point is found further northward of the equator, at $z \approx 1.8\ R_E$ in the noon meridian plane, as shown in Figure 4c. On the other hand, in Figure 4d under a sunward dipole tilt (Tan et al., 2011), there is an X line southward of the equator at $z \approx -1.4\ R_E$ in Case (d).

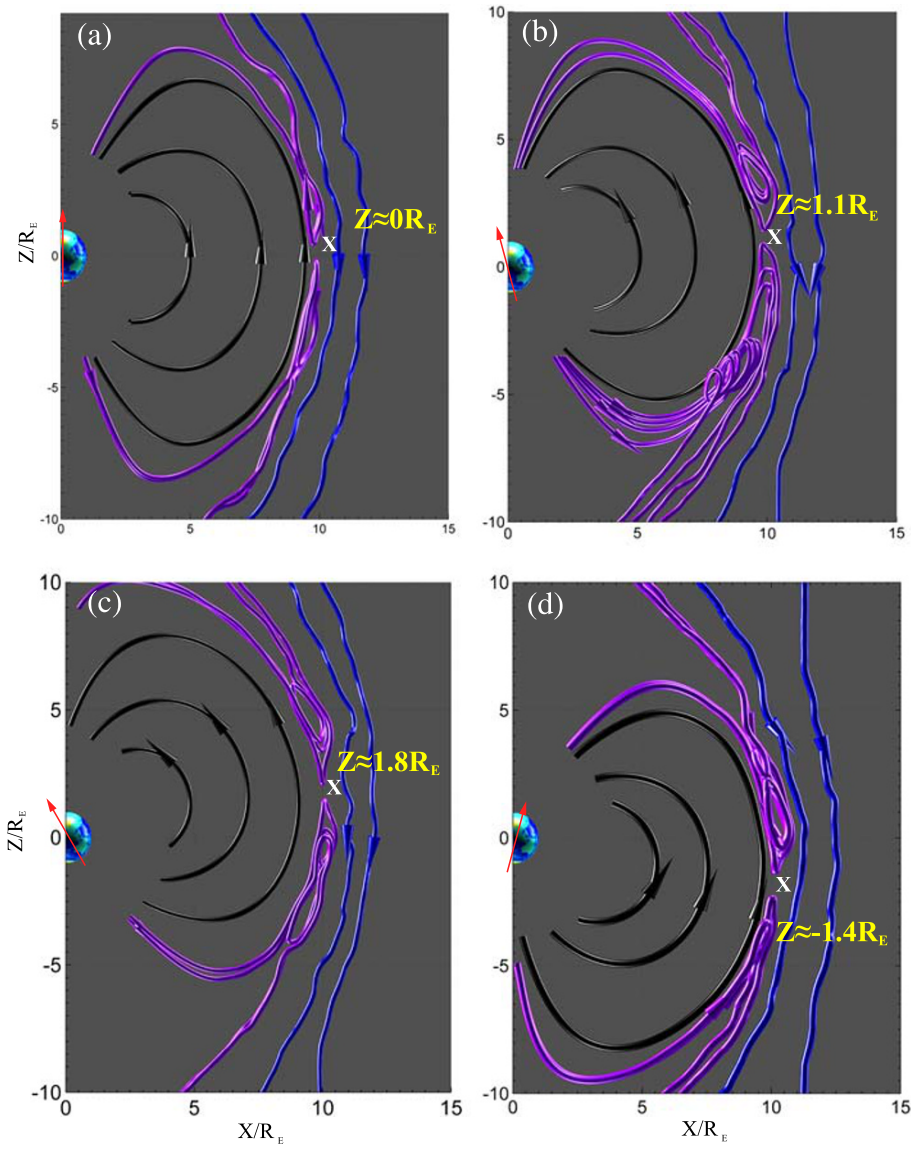

Figure 4. Magnetic field line configuration in the noon meridian plane obtained in cases in which the Earth's dipole tilt angle is equal to (a) 0°, (b) −15°, (c) −27°, and (d) 15°. The red arrow in each plot indicates the direction of the dipole moment. The field lines are denoted by color lines. The white "X" denotes the magnetopause subsolar X line location.

The ion diffusion region around the X line of reconnection can be identified by spatial variations of the electric field, as well as the contributions of terms in the generalized Ohm's law in the reconnection region, as shown in Figure 5. Figure 5a depicts the zoomed-in contour plot of the component B_y in the noon meridian plane, from $x = 8.0\ R_E$ to $12.0\ R_E$ and from $z = -2.0\ R_E$ to $6.0\ R_E$ at $t = 20.0\Omega_{i0}^{-1}$. The black lines superposed on the contours are the field lines projected onto the plane. Figure 5b shows the spatial variations of the electric field components E_x, E_y, and E_z (in black color), as well as the contributions of the Hall term $(J \times B)/eN$ (red), the ion convection term $-V_i \times B$ (blue), the collision term $-\upsilon(V_e - V_i)$ (green), where V_e is the electron flow velocity, and the electron pressure gradient term $-\nabla P_e/\mathrm{eN}$ (yellow) in the generalized Ohm's law, obtained from the hybrid simulation, along the Line L1 across the outflow region (marked in Figure 5a). The corresponding line cut results along the Line L2 through the X point region (see Figure 5a) are plotted in Figure 5c. The term $E+V_i \times B$ is plotted in the black dashed curves. In the magnetopause boundary region, $E + V_i \times B \neq 0$ is seen between the two vertical black dashed lines, where E_x is seen to points into the current layer from both the magnetospheric and magnetosheath side due to the Hall physics associated with charge

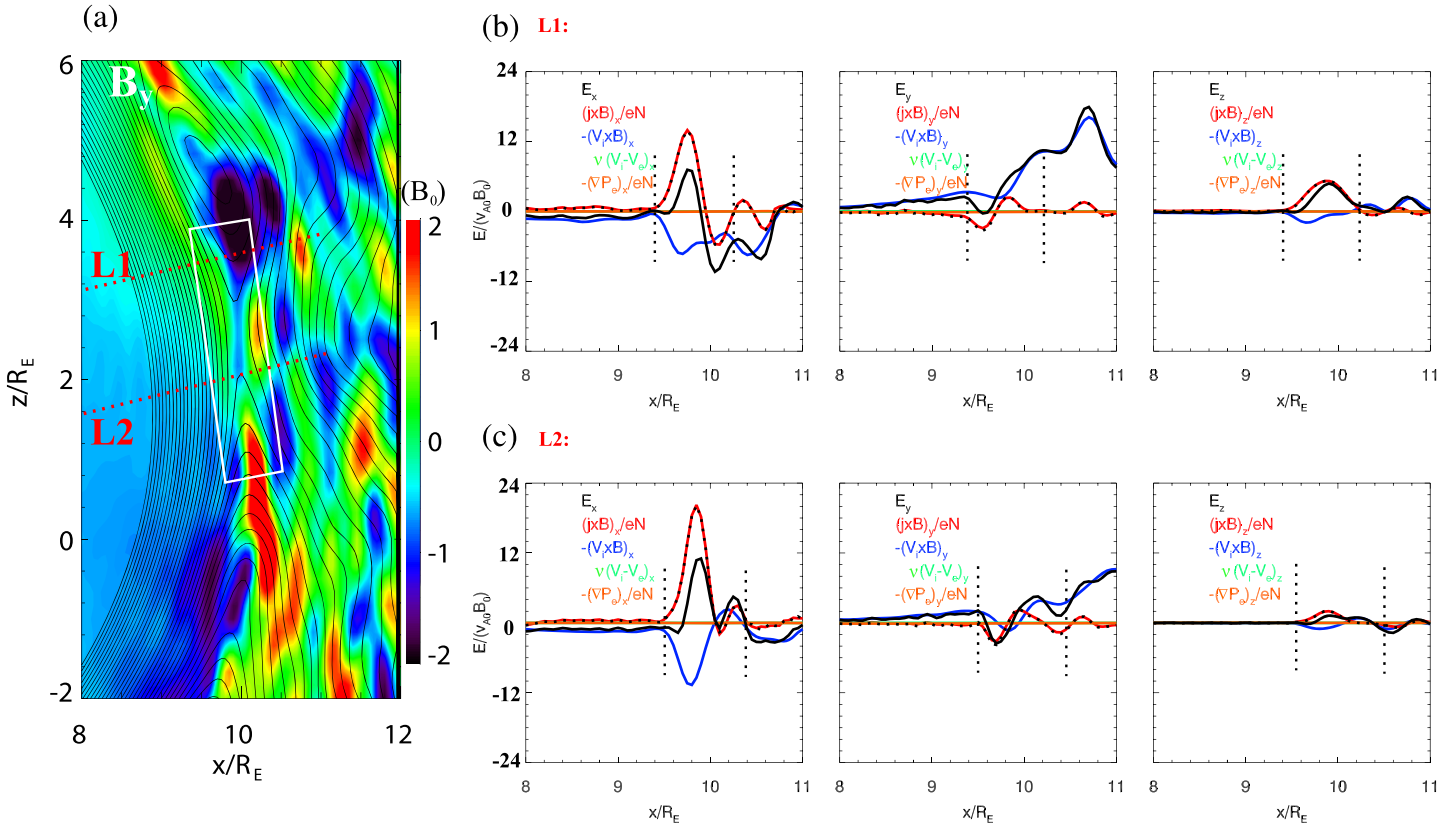

Figure 5. (a) Zoomed-in contour plots of the B_y component in the noon meridian plane, from $x = 8.0\ R_E$ to 12.0 R_E and $z = -2$. R_E to 6.0 R_E at $t = 20.0\Omega_{i0}^{-1}$. The white rectangle shows the ion diffusion region, above the equator. (b and c) Spatial variations of (left) E_x, (middle) E_y, and (right) E_z as well as the contributions of the Hall term $(J \times B)/eN$ (in red), the convection term $-V_i \times B$ (in blue), the resistive term $-\upsilon(V_e - V_i)$ (in green), and the electron pressure gradient term $-\nabla P_e/eN$ (in yellow) in Ohm's law along the Lines (b) L1 and (c) L2 marked in (a). The term $E + V_i \times B$ is plotted with the black dashed curves.

separation. The corresponding charge separation effect leads to an $E_z > 0$ (on the northward side of the X line). This is the region in which the ion motion is decoupled with that of the magnetic field lines, and thus, the ion convection term and the Hall term of the electric field are comparable. The width of this ion diffusion regions marked by the white rectangle in Figure 5a is found to be ~0.8 R_E.

The overall structures of various physical quantities around the magnetopause multiple X lines are shown in Figure 6, which depicts the zoomed-in contour plots of the magnetic field strength B (Figure 6a), component B_y (Figure 6b), ion density N (Figure 6c), ion temperatures $T_{\|}$ (Figure 6d) and $T_{\perp}$ (Figure 6e), and ion bulk flow component V_{iz} (Figure 6f) in the noon meridian plane, from $x = 8.0\ R_E$ to 12.0 R_E and from $z = -2.0\ R_E$ to 6.0 R_E at $t = 20.0\Omega_{i0}^{-1}$. The black lines superposed on the contours are the field lines projected onto the two-dimensional (2-D) noon meridian plane. The location of FTEs can be identified from the magnetic islands traced by the field lines in the contour plots. The white rectangle in each plot shows the ion diffusion region of the reconnection event above the equator (see Figure 5a), while the position of the corresponding X line reconnection point in the white rectangular region is marked with a white arrow in Figure 6b. Quadrupolar perturbations denoted by the signs of positive and negative B_y are present in the vicinity of the X line, as seen in the white rectangle in Figure 6b, which is consistent with the Hall effects due to the ion kinetic effects (Pritchett, 2001; Tan et al., 2011; Terasawa, 1983). The Hall magnetic field perturbations with $\delta B_y \sim 2.0B_0$ on the magnetosheath side of the reconnection region are much stronger than that ($\delta B_y \sim 0.2B_0$) on the magnetospheric side due to the much larger ion density on the magnetosheath side, leading to an asymmetric quadrupole structure at the magnetopause. The thickness of the quadrupole δB_y region on the magnetosheath side is about 0.2–0.5 R_E. Figure 6c reveals that the FTEs are associated with an ion density enhancement at the core. Corresponding to the density enhancement, the magnetic field strength is

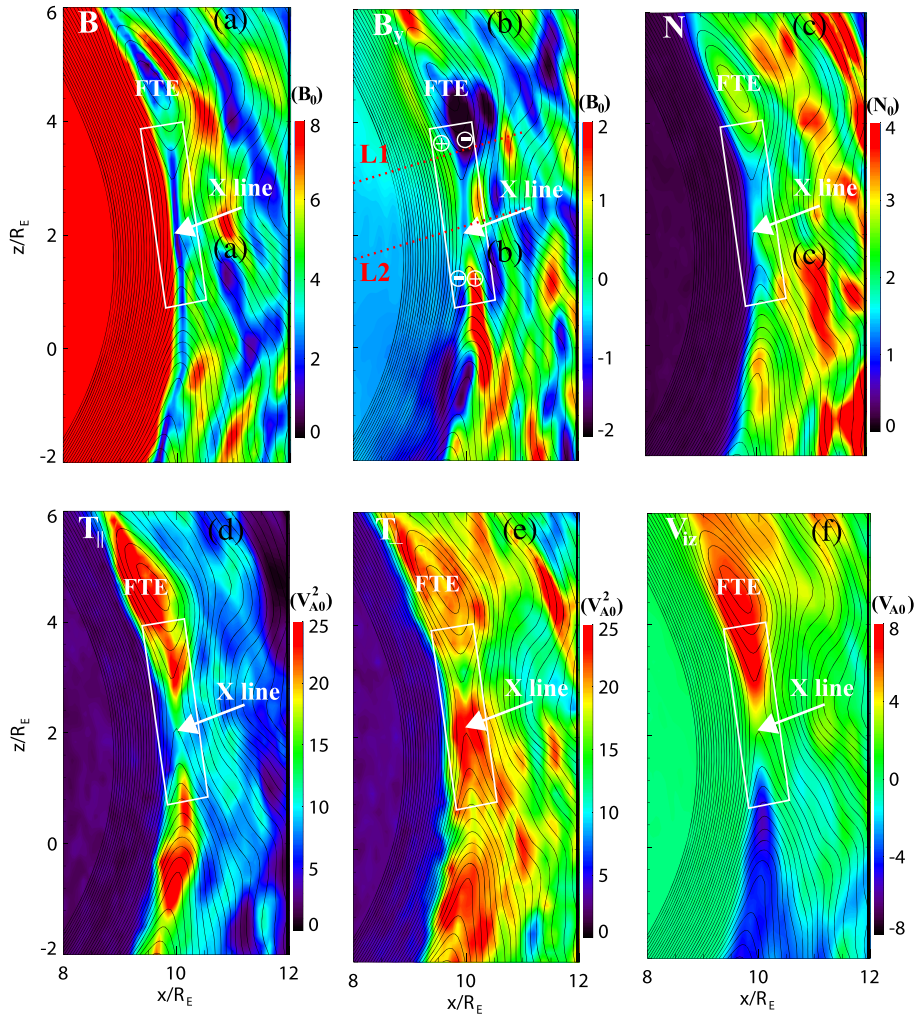

Figure 6. Zoomed-in contour plots of (a) the magnetic field strength B, (b) B_y component, (c) ion density N, (d) ion parallel temperatures $T_{\parallel}$, (e) perpendicular temperatures $T_{\perp}$, and (f) ion bulk flow component V_{iz} in the noon meridian plane, from $x = 8.0\ R_E$ to $12.0\ R_E$ and $z = -2.\ R_E$ to $6.0\ R_E$ at $t = 20.0\Omega_{i0}^{-1}$. The white rectangle highlights the ion diffusion region in the vicinity of X line.

found to dip in the core of the FTEs, as seen in Figure 6a. The presence of two reconnection jets, pointing away from the X line, can be seen from the z component of ion bulk flow velocity V_{iz} in Figure 6f. One jet moves northward with a speed of ~$4.0V_{A0}$ in the outflow region, and the other one moves southward with a speed of ~$-3.2V_{A0}$. As the latitude increases, the $|V_{iz}|$ flow in the magnetosheath increases. Temperature enhancement is found in the core of the FTEs, as shown in Figures 6d and 6e.

To examine the global structure of the dayside reconnection X lines at various times, Figure 7a presents the reconnected field lines (white and orange lines) near the paraboloidal-shaped magnetopause at $t = 20.0\Omega_{i0}^{-1}$, $30.0\Omega_{i0}^{-1}$, and $40.0\Omega_{i0}^{-1}$, where the white and orange lines denote the reconnected field lines moving northward and southward, respectively. Figure 7b shows isosurface plots of V_{iz} superposed on the same field line plots as Figure 7a. In Figure 7b, the red patches mark the ion bulk flow speed of $V_{iz} = 3.2V_{A0}$, and the blue patches indicate $V_{iz} = -2.8V_{A0}$. The dashed black, blue, and red lines in Figure 7 indicate the positions of the three dominant X line segments in the magnetopause close to the equatorial region, which are seen on the duskside, northward of the equator near the subsolar region, and on the dawnside, respectively. Bidirectional ion bulk flows are clearly seen on the two sides of the X lines, as shown in Figure 7b, giving a 3-D perspective of the flow structure around an X line as discussed in Figure 6. Note that the jet speeds

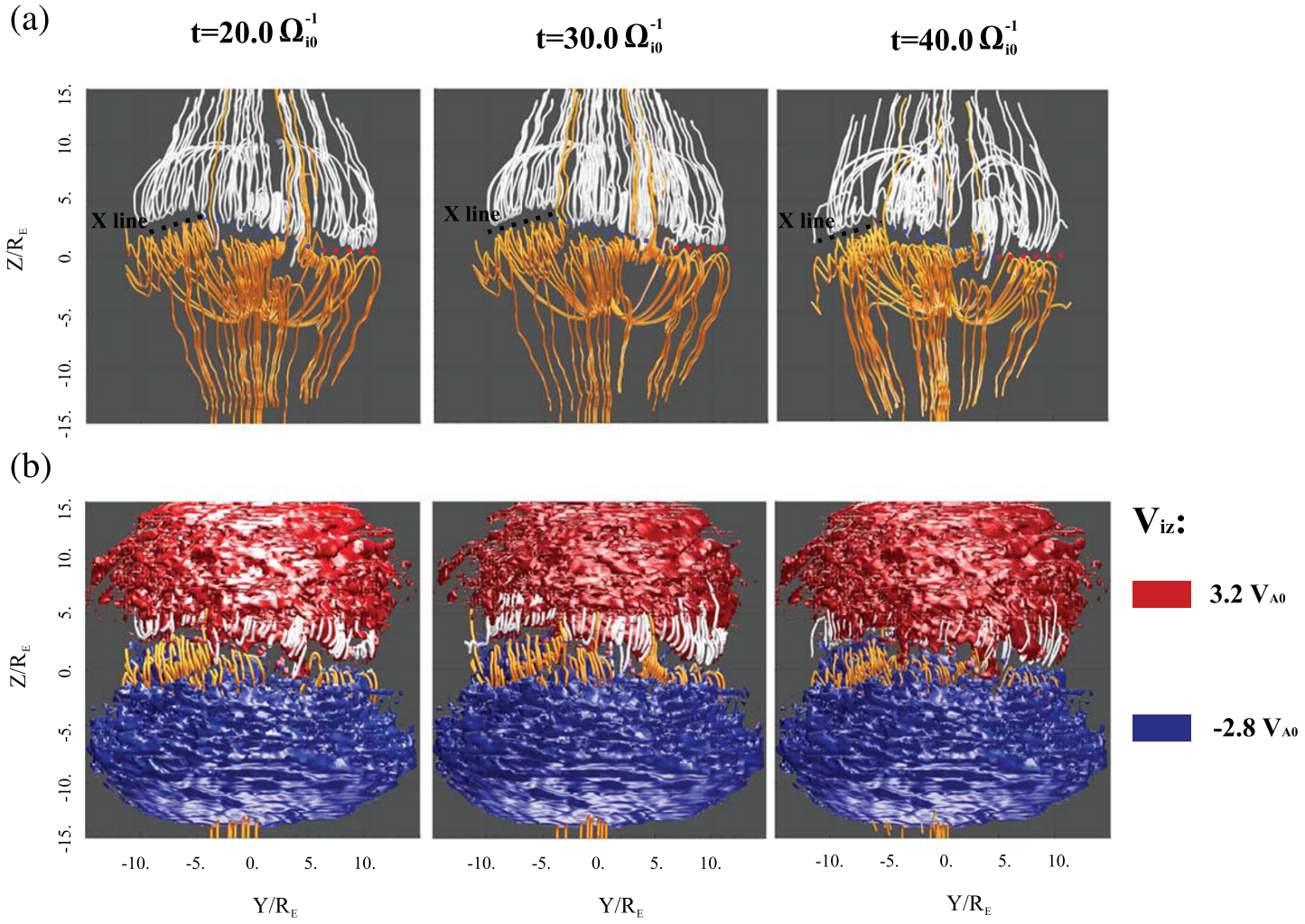

Figure 7. (a) Contour plots of magnetic field line configuration at the magnetopause and (b) isosurface plots of $V_{iz} = 3.2V_{A0}$ (red patch) and $V_{iz} = -2.8V_{A0}$ (blue patch), obtained at $t = 20.0\Omega_{i0}^{-1}$, $30.0\Omega_{i0}^{-1}$, and $40.0\Omega_{i0}^{-1}$. The white and orange lines are reconnected field lines (flux ropes) moving northward and southward at the magnetopause. The dashed colored dashed lines indicate the magnetopause subsolar X line location in Figure 7a.

are different at different X point locations and at different times. At $t = 20.0\Omega_{i0}^{-1}$, the two opposite ion jets flow with speeds of $V_{iz} \sim 3.0V_{A0}$ and $\sim -3.0V_{A0}$ on the duskside, about $4.0V_{A0}$ and $-3.2V_{A0}$ around the subsolar region, and about $3.4V_{A0}$ and $-2.6V_{A0}$ on the dawnside. Scaled to V_A (where $V_A = B/\sqrt{\mu_0 m_i N}$ is the local Alfvén speed), the opposite flow jets in general have a speed of ~0.6 V_A to 1.2 V_A. It is noted that the X lines are also moving, as to be illustrated below.

Meanwhile, multiple X lines are present northward and southward of the near equator X lines. The magnetopause reconnection regions are located at middle latitudes in the northern dawn region, around noon, and at low latitudes in the dusk region near the equator. It is found that, over the time, the positions of the X lines oscillate around similar locations and the overall global distribution of the magnetopause X line configuration remains unchanged, extending nearly along the *y* direction, with the near-subsolar X line located northward of the equator. In the dynamic evolution, a subsolar X line form above the equator and then be swept poleward. A new X line then re-forms around the same location as the current sheet there is stretched thinner. A looped flux rope is created between the two neighboring X lines, corresponding to MXR. Magnetic flux ropes (i.e., FTEs) and X lines form repeatedly and propagate poleward along the magnetopause boundary layer. It is found that the dayside reconnection is not in a steady state even though the solar wind parameters are kept constant.

To illustrate the motion of the reconnection site and magnetic flux ropes, Figures 8a and 8c show the magnetic field strength in the noon meridian plane at $t = 20.0\Omega_{i0}^{-1}$ and $25.0\Omega_{i0}^{-1}$, respectively, while the corresponding typical field lines at $t = 20.0\Omega_{i0}^{-1}$ and $25.0\Omega_{i0}^{-1}$ are depicted in Figures 8b and 8d, respectively. Two X sites of reconnection are found for these times, marked by the black cross and the red triangle. At $t = 20.0\ \Omega_{i0}^{-1}$ (in Figures 8a and 8b), a localized looped magnetic flux rope centered at $(x, z) = (9.0,4.8)R_E$ is found in between two neighboring X lines, marked by the orange field line. The two X sites at $t = 20.0\Omega_{i0}^{-1}$ are marked by the white line segments in Figure 8a, located at $(x,z) = (9.967,1.785)\ R_E$ and $(x, z) = (8.815,6.159)\ R_E$, indicated by the red triangle and the black cross in Figure 8b, respectively. At $t = 25.0\Omega_{i0}^{-1}$ (Figures 8c and 8d), the looped flux rope illustrated by the orange field line of $t = 20.0\Omega_{i0}^{-1}$ has moved northward/poleward along the magnetopause boundary, as indicated by the white arrow in Figure 8c, with the center of the flux rope now located at $(x, z) = (8.5,6.8)\ R_E$. The two reconnection X sites have moved to $(x, z) = (9.651,3.657)\ R_E$ and $(x,z) = (7.638,7.683)\ R_E$, marked by the red triangle and the black cross in Figure 8d. As a reference, the two white lines in Figure 8a are plotted again in Figure 8c at the initial position. The average speed of the X lines is found to be nearly $3.2V_{A0}$ in the time interval of $t = 20.0\Omega_{i0}^{-1}$ to $t = 25.0\Omega_{i0}^{-1}$, comparable with the average magnetosheath flow speed of $3.0V_{A0}$. But the speed of X lines is, in general, time dependent. Neighboring reconnection sites and X lines could modify the local plasma conditions at the magnetopause, for example, by the formation and propagation of magnetic flux ropes, which further influences the reconnection rate. Therefore, both the magnetosheath flows and the outflow structures associated with the multiple reconnection sites may play important roles in the displacement of the X lines.

Figure 9 shows the x and z positions of the centers of 12 subsequently formed flux ropes as a function of time. The FTEs due to multiple X line reconnection move poleward and tailward away from their positions of origin near the subsolar magnetopause. The flux rope moving at a speed $3.2V_{A0}$ from $t = 20.0\Omega_{i0}^{-1}$ to $t = 25.0\ \Omega_{i0}^{-1}$ is marked by "FR1" in the figure. The speed of the flux rope marked by "FR2" is ~0.2 V_{A0} in the time interval of $t = 25.0\Omega_{i0}^{-1}$ to $t = 40.0\Omega_{i0}^{-1}$, slower than the magnetosheath flow. While the speed of the flux ropes is time dependent, the average locations of the magnetopause subsolar X lines are nearly the same. The flux ropes ultimately move tailward out of the domain. The propagation of X lines is also discussed in the work of Sibeck and Omidi (2012), which shows that the FTEs ultimately disintegrate into the cusp. In our case, the northern cusp is outside the domain.

Since the magnetosheath waves just outside magnetopause may also influence the magnetopause reconnection, we present magnetosheath waves as an important part of the self-consistent global physics. In this case of the quasi-perpendicular bow shock, mirror mode waves are found and revealed from our 3-D global simulation. These waves in our simulation exhibit an anticorrelation between fluctuations in the magnetic field and the ion density. Our analysis shows that these waves are mirror mode waves. In this study we use the same criteria for mirror mode waves as those used by Génot et al. (2009) and Soucek et al. (2008) to test the magnetosheath waves. The relative fluctuations are defined as $\delta B/B = (B - < B>)/ < B>$ and $\delta N/N = (N - < N>)/ < N>$, where <> marks the time average over the time period from $t = 30.0\Omega_{i0}^{-1}$ to $80.0\ \Omega_{i0}^{-1}$. Figures 10a–10c show the zoomed-in contour plots of the magnetic field strength B (Figure 10a), ion density N (Figure 10b), and ion temperature ratio $T_\perp/T_\parallel$ in the noon meridian plane, from $x = 9.0\ R_E$ to $14.0\ R_E$ and $z = -5.0\ R_E$ to $5.0\ R_E$ at $t = 40.0\Omega_{i0}^{-1}$. The short white lines in Figures 10a–10c mark the positions of antiphase fluctuations between the magnetic field and ion density. Figure 10d shows the time evolution of the proton pressure anisotropy ratio $P_\perp/P_\parallel$, relative fluctuations in magnetic field ($\delta B/B$) and ion ($\delta N/N$), and the angle (θ_{Bm}) between the maximum variance direction and the background magnetic field at position marked by "A" in Figures 10a–10c, where $P_\parallel$ and $P_\perp$ are the perpendicular and parallel ion thermal pressure, respectively. The black line in Figure 10d marks the proton pressure ratio ($P_\perp/P_\parallel$) obtained in the hybrid simulation (marked as Hyb), while the dashed blue line marks the mirror mode stability criterion ($(P_\perp/P_\parallel)_{Mir} = 1+1/\beta_\perp$; A. Hasegawa, 1969). At the quasi-perpendicular shock front, the ratio $P_\perp/P_\parallel$ increases strongly and abruptly because particles from the superfast solar wind undergo a specular gyration around the magnetic field. Large-amplitude in-phase oscillations of B and N are seen near the bow shock transition, which are of the quasi-perpendicular magnetosonic/fast mode (not shown). About 1.0 R_E away from the shock transition, $P_\perp/P_\parallel$ decreases to a moderate value, and antiphase oscillations between B and N are

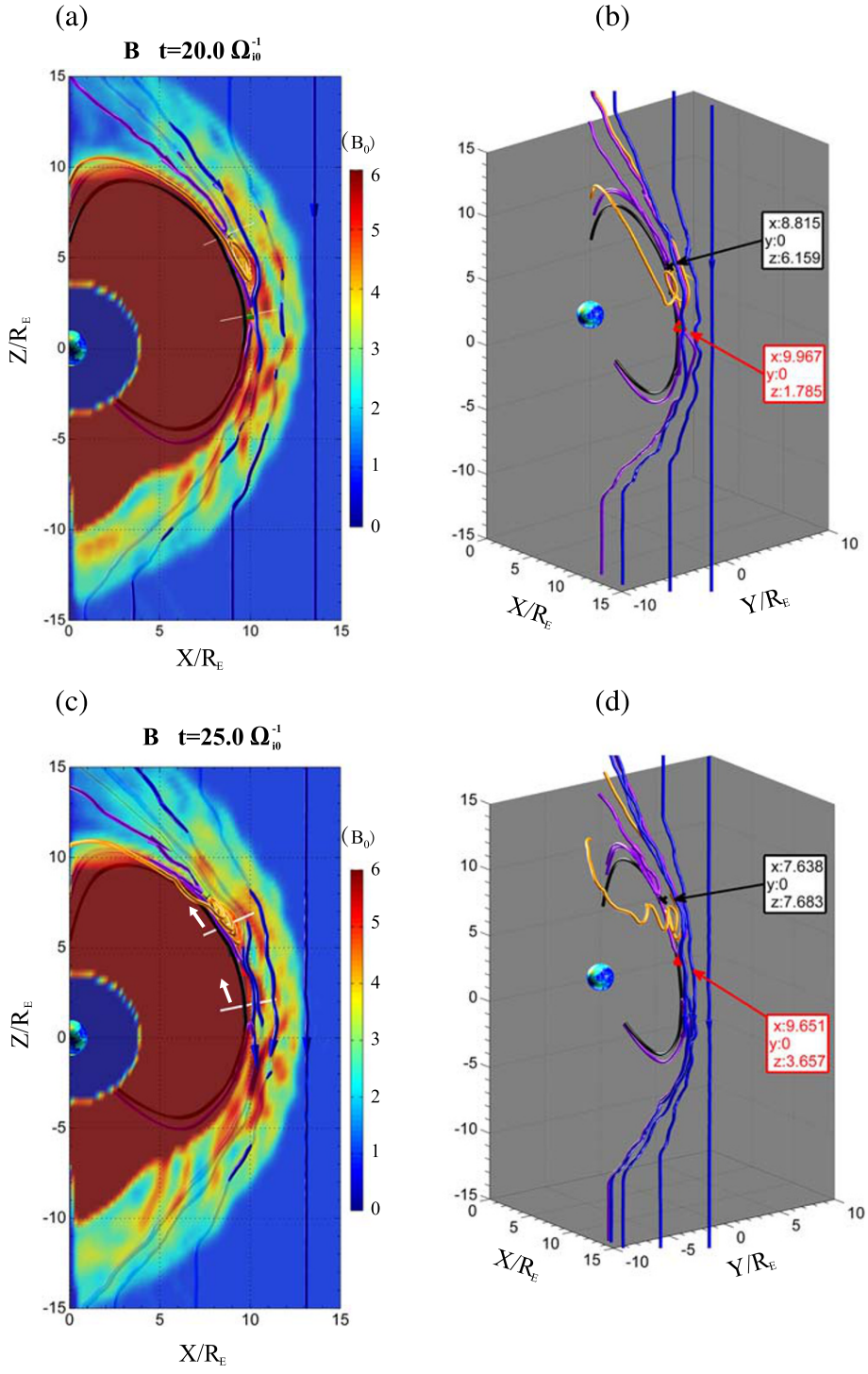

Figure 8. Contours of the magnetic field strength B in the noon meridian plane obtained at (a) $t = 20.0\Omega_{i0}^{-1}$ and (c) 25.0 Ω_{i0}^{-1}, with the corresponding typical field lines around the magnetopause at (b) $t = 20.0\Omega_{i0}^{-1}$ and (d) $25.0\Omega_{i0}^{-1}$. The black crosses and the red triangles indicate two reconnection sites in the noon meridian plane. The short white lines mark the positions of these two X lines at $t = 20.0\Omega_{i0}^{-1}$ in the noon meridian plane. The white arrows indicate the propagation of flux ropes (seen on orange field lines) and the reconnection sites.

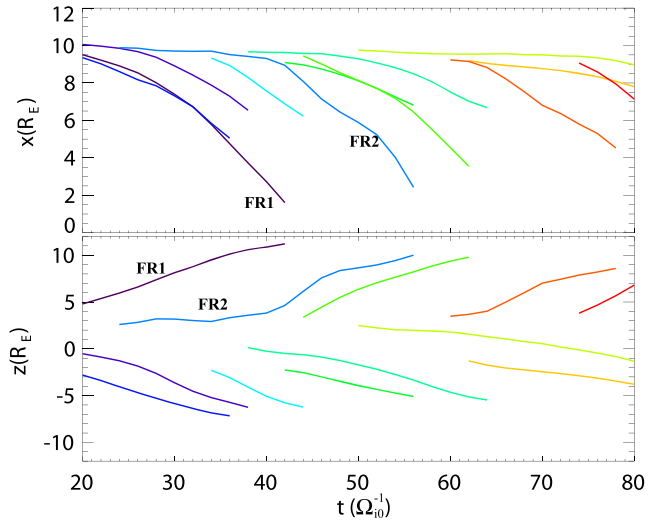

Figure 9. Locations of (up) x and (down) z for 12 subsequently formed flux ropes, marked by different colored curves, as a function of time in the simulation.

present. In this region in the midmagnetosheath, the ratio $P_{\perp}/P_{\parallel}$ stays above or near the marginal stability condition of the mirror mode wave (marked as Mir, blue dash-dotted line in Figure 10d). The angle between the maximum variance direction and the mean magnetic field ranges between about 3° to 8°, smaller than 20°, and the variance of the field is much larger than 10%. These waves with the antiphase oscillations between B and N are identified as mirror mode waves (Génot et al., 2009; Soucek et al., 2008).

3.2. Detailed Results: Data-Model Comparison

To compare the simulation results with the in situ measurements from MMS-3 spacecraft, we first identify three distinct regions of the outer magnetosphere, magnetopause, and magnetosheath from MMS observations. The three regions at the magnetopause are identified by the magnetic field direction and ion fluxes and moments as shown in Figure 11. The outer magnetosphere is characterized by a higher B magnitude with a dominant positive B_L component, lower ion density and flow speed, higher ion fluxes at energies above a few keV (but with a separate ion population below ~50 eV), and much higher ion temperatures than seen after 02:15 UT. The magnetopause current layer encompasses the rotation in the magnetic field from strongly positive to strongly negative B_L as shown in Figure 11a, with increasing ion density (in Figure 11e), a large negative enhancement in the ion V_L component (in Figure 11g), and ion temperatures (in Figure 11f) between that seen before 01:50 and after 02:15 UT. The magnetosheath is characterized primarily by the negative B_L component, much higher ion densities, lower ion temperatures, and much greater ion fluxes at energies of ~50 eV to ~2 keV than seen before 02:10 UT. The magnetosheath and magnetopause current layer are also differentiated from the magnetospheric region by the presence of high fluxes of solar wind He^{++} ions at energies of tens of eV to a few keV, seen in observations from the Hot Plasma Composition Analyzer (Young et al., 2016) (not shown). This magnetopause crossing interval is characterized by a fairly large, but not purely antiparallel, local magnetic shear angle of 147°, indicating some contribution to the reconnection X line across the dayside from a guide field component, as well as a relatively low $\Delta\beta$ ($\Delta\beta$=$|\beta_{sheath} - \beta_{spere}|$, where $\beta = 2\mu_0 N_i k T_i / B^2$) of 1.11, indicating more symmetric plasma conditions than normally seen at the dayside magnetopause with nominal solar wind and IMF values (see Cassak & Fuselier, 2016).

In order to make a comparison with the MMS observations, we increase the time t presented here by a factor 8.2 for the hybrid simulation, considering the scaling factor associated with a faster wind speed used in the simulation while keeping a realistic Ω_{i0}. In addition, since the preconditions in the simulation are arbitrary, we align $t = 627.3$ s in the simulation with 02:13:00 UT in the MMS-3 observation (marked by the orange vertical line in Figure 13) so that the center of our simulated magnetopause current sheet is aligned with that of the MMS-3 observation on the basis of the magnetic field strength or the (predominant) B_L component of magnetic field. The comparison is conducted for the MMS-3 magnetopause event from 02:10 to 02:16 UT. The LMN coordinate system can be obtained in our hybrid simulation using the minimum variance analysis (Sonnerup & Scheible, 1998) applied to this period. The positive N axis is obtained as (0.9601, −0.2222, −0.0967) (GSM), pointing toward the Sun. The L axis is along (0.1495, 0.2105, 0.9667) (GSM), which is defined as the reconnection magnetic field direction in the plane of the magnetopause current sheet, and the M axis, (−0.206, −0.9587, 0.1583) (GSM), completes the right-handed orthogonal system. The local LMN coordinates obtained in the simulation are roughly consistent with the boundary normal coordinates of L = (0.1974, 0.2013, 0.9594), M = (−0.1170, −0.9669, 0.2269), and N = (0.9733, −0.1570, −0.1673) obtained from the MMS-3 spacecraft.

To illustrate the locations of the subsolar reconnection site in our hybrid simulation and the MMS-3 observation, Figure 12 shows the configuration of magnetic field lines in a global view. The colored sphere at the origin represents the Earth. In addition, the colored contours in Figure 12 show the magnetic field strength in the xz plane at $y = -1.0\ R_E$ at $t = 627.3$ s. Three colors of the magnetic field lines are shown in this figure, with the black ones being the closed dipole-like field lines, the violet and orange field lines showing the

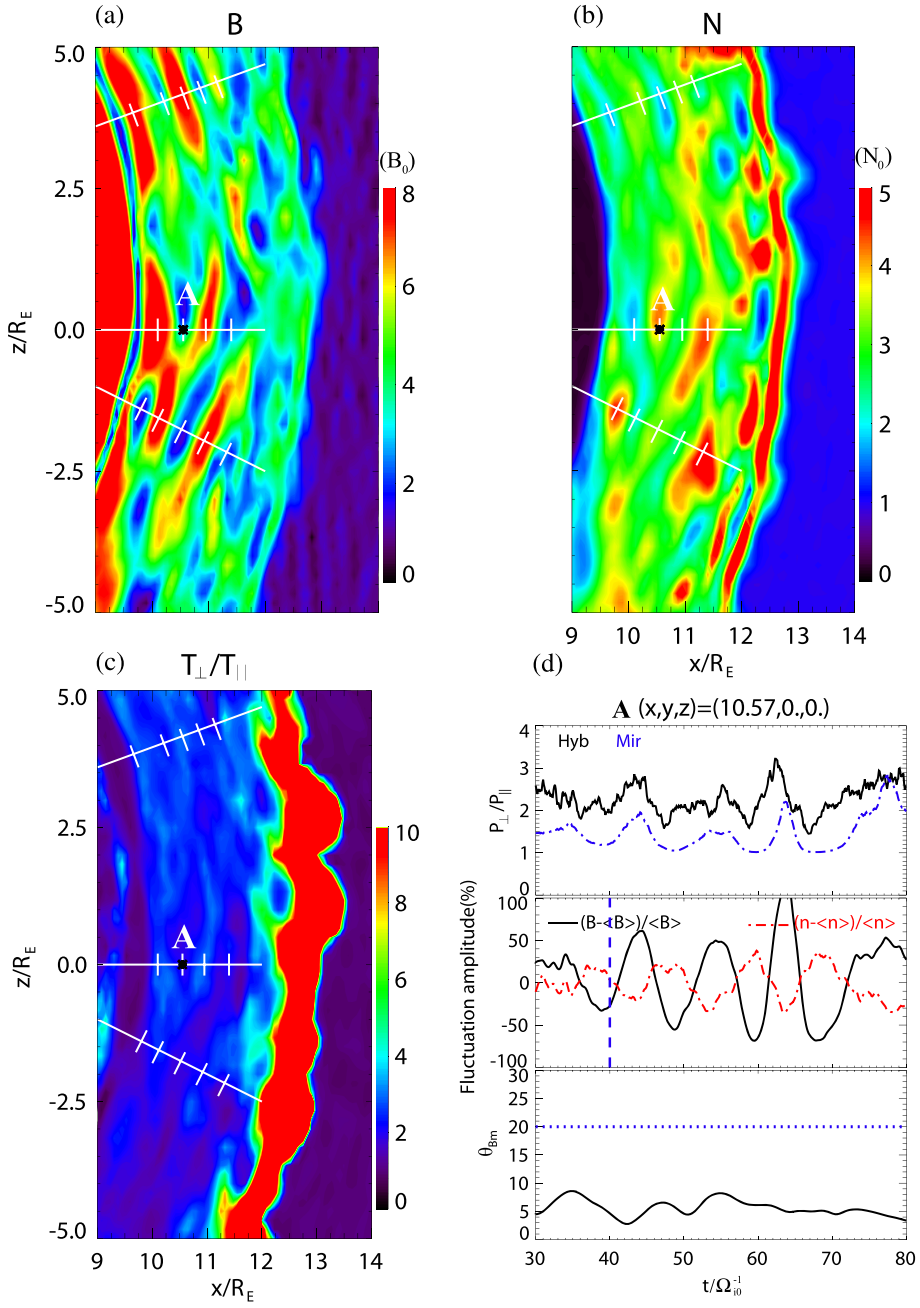

Figure 10. Zoomed-in contour plots of (a) the magnetic field strength B, (b) density N, and (c) ion temperatures ratio $T_\perp/T_\parallel$ in the noon meridian plane, from $x = 9.0\ R_E$ to $14.0\ R_E$ and $z = -5.0\ R_E$ to $5.0\ R_E$ at $t = 40.0\Omega_{i0}^{-1}$. (d) Time variations of ion pressure ratio $P_\perp/P_\parallel$ (black: hybrid simulation results; blue: analytical criterion of mirror mode instability), relative fluctuations in the magnetic field ($\delta B/B$) and ion density ($\delta N/N$), and angle (θ_{Bm}) between the maximum variance direction and the background magnetic field in the midmagnetosheath at position marked by "A" in Figures 10a–10c.

reconnected field lines at the magnetopause, and the blue ones representing the open field lines in the magnetosheath and solar wind. The arrows in Figure 12 display the directions of the local magnetic field. The field line in orange shows a magnetopause flux ropes generated by reconnection. The MMS-3 spacecraft and magnetopause reconnection locations are marked with a white star and white circle, respectively. The configuration of the field lines at the magnetopause indicates that there is a reconnection site (X line) at $z \approx 1.92\ R_E$ above this virtual satellite location, as seen in Figure 12. This is

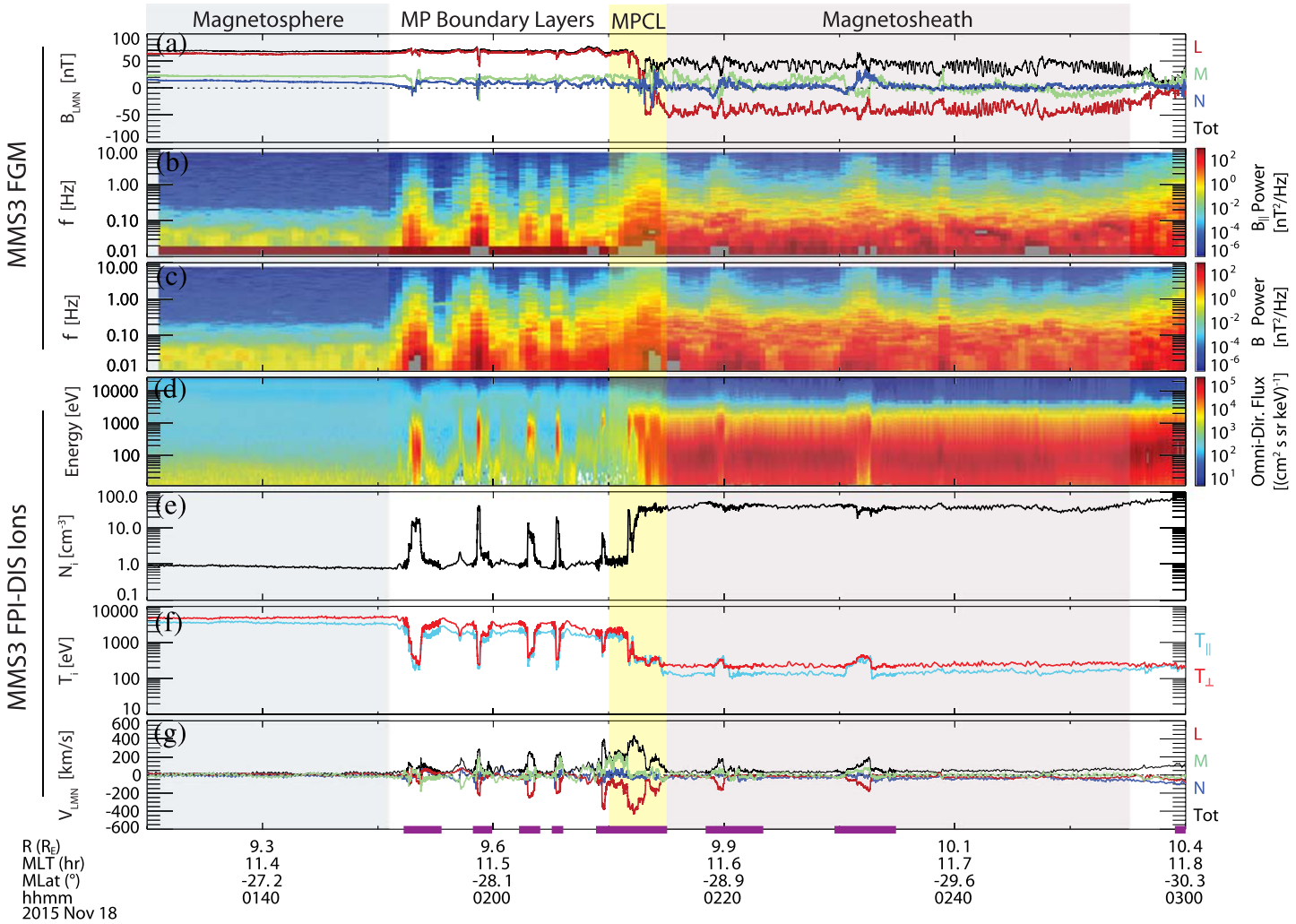

Figure 11. (a) Magnetic field B_{LMN}, (b) parallel magnetic field component wave power spectrum, (c) perpendicular magnetic field component wave power spectrum, (d) omnidirectional ion differential flux, (e) ion density N_i, (f) ion temperatures T_i, and (g) ion bulk velocity V_{LMN} observed by the MMS-3 spacecraft. The magnetic field and ion bulk velocity data are shown in LMN coordinates. The red, green, and blue curves indicate the L, M, and N components, respectively. The magnitude of magnetic field and ion velocity is shown as the black curve. The blue and red curves in Figure 10f indicate the ion parallel and perpendicular temperature components, respectively. The purple bars at the bottom of panel (g) indicate times of burst mode data. The shaded areas denote the distinct regions of the magnetosphere, magnetopause current layer (MPCL), and magnetosheath.

consistent with the estimated reconnection X location from the MMS and Geotail observations, inferred to be northward of MMS at GSM $z \approx 2.0\ R_E$ (Kitamura et al., 2016). For the sake of comparison between the observations and our simulation, we impose a virtual spacecraft along the MMS-3 spacecraft orbit marked by a white star.

We now compare the hybrid simulation results with measurements from the MMS-3 spacecraft. Figure 13 shows the magnetic field strength B (Figure 13a), component B_L (Figure 13b), B_M (Figure 13c), B_N (Figure 13d), ion bulk flow velocity V_L (Figure 13e), V_M (Figure 13f), V_N (Figure 13g), and ion density N (Figure 13h) during the period of the magnetopause crossing from 02:10 to 02:16 UT as a function of time. During the time interval, the virtual spacecraft in the hybrid simulation is positioned roughly at the fixed location but having a very small displacement with time as that of MMS-3. The observational results are displayed with the black lines, and the hybrid simulation results are plotted by the red line (labeled Hybrid_aligned). As a comparison, results based on global simulations with the MHD with embedded PIC (MHD-EPIC) model are also shown in Figure 13 by blue lines; the MHD-EPIC simulation is also conducted for the GEM Dayside Kinetic Challenge for the same MMS magnetopause event (see Chen et al., 2020, in the

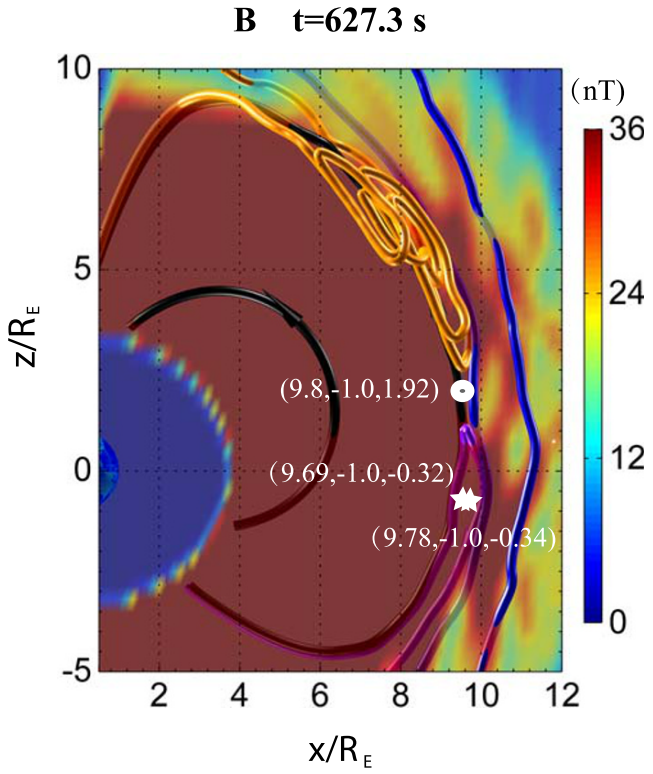

Figure 12. Colored solid lines depict the field line configuration around the magnetopause in the noon meridian plane obtained from the hybrid simulation at $t = 627.3$ s. Four colors of the magnetic field lines are closed (black), reconnected (orange and violet), and open (blue) magnetic field lines at the magnetopause. The colored contours show the magnitude of magnetic field in the xz plane at $y = -1.0\ R_E$ at $t = 627.3$ s. The colored sphere at the origin represents the Earth. The MMS-3 spacecraft and magnetopause reconnection locations are marked with white stars and a white circle, respectively.

same issue for details). In both the hybrid and the MHD-EPIC simulations, unrealistically large particle Larmor radii (or inertial lengths) are used, which also correspond to a smaller ratio between the global convections and the particle gyroperiod. Recall that for hybrid simulation, the time is scaled by a factor of 8.2. The scaling of the MHD-EPIC results is based on the distance being 16 times larger than reality. Note that the LMN directions in the hybrid simulation results are obtained from the self-consistent simulation data, while the LMN coordinates used in the MHD-EPIC model are based on the MMS3 observation results (Kitamura et al., 2016). We mainly focus on the comparison between the hybrid simulation and the MMS observation in the following paragraphs.

As shown in Figures 13a and 13b, the magnetic field appears to be dominated by the B_L component around the time of the magnetopause crossing in both the observation and the simulation. During the time period from 02:10 to 02:16 UT, the MMS-3 experiences a full and a partial magnetopause crossing. A full magnetopause crossing at ~02:13:00 can be identified by change of the sign of B_L from positive (magnetosphere) to negative (magnetosheath) in both the observation and the simulations, as seen in Figure 13b. A partial magnetopause crossing event is found at 02:11:30 UT in the observation, indicated by the increase of the ion density (see also Figure 11), but not in the simulations. In the observation at 02:11:30 UT, the B_L component of the magnetic field (in Figure 13b) decreases but does not change sign. This signifies that the MMS-3 spacecraft does not fully cross the magnetopause current sheet but enters into it and then returns back to the magnetospheric side of the magnetopause due to magnetopause oscillation. The magnitude of the field strength inside the magnetopause is generally stronger than that in the magnetosheath in the asymmetric dayside reconnection. Based on the results summarized by Figures 13a, 13b, and 13d, the overall trend of oscillations in B, the dominant component B_L, and the B_N component obtained in our hybrid (as well as the MHD-EPIC) simulations show resemblance to that observed by MMS-3 spacecraft.

MMS-3 observed significant positive components of B_M in the magnetosheath in Figure 13c, but the B_M component in the hybrid simulation does not resemble the observed value. In addition, the observed B_M component in Figure 13c has significant variations, but none of the simulations capture these structures. The difference in the B_M component may be resulted from the simplified upstream of IMF condition ($B_y = 0$) used in the simulation. In addition, a finite B_M of quite substantial amplitude is shown in Figure 13c in the asymptotic magnetospheric part of the MMS crossing, but not in the hybrid simulation. This discrepancy between the simulation and the observation is because that the distance of the virtual spacecraft location in the simulations relative to the magnetopause is not exactly the same as that of the MMS-3 spacecraft. If we shift our virtual spacecraft location inward by 0.06 R_E, that is, to a slightly different range of $x = 9.63$ to 9.78 R_E, a finite B_M is present on the asymptotic magnetosphere side, as shown by the purple line in Figure 13c (labeled by Hybrid_adjusted). There appear to be more small-scale oscillations in the MHD-EPIC simulation than in the Hybrid simulation, since the PIC model in the MHD-EPIC simulation can capture higher frequency electron physics (Chen et al., 2020). Also for the M-component, the MMS observed a significant positive component of V_M in the magnetosphere, which is not shown in the simulations.

In Figure 13e, a southward ion flow jet with a speed of >300 km/s is found in both the observation and the simulations during this magnetopause current layer crossing. This flow acceleration appears around 2:12:45 UT on the simulation curve. The fast southward flow indicates that there is a reconnection X line or site located northward of the observation point, which in our simulation is located at GSM

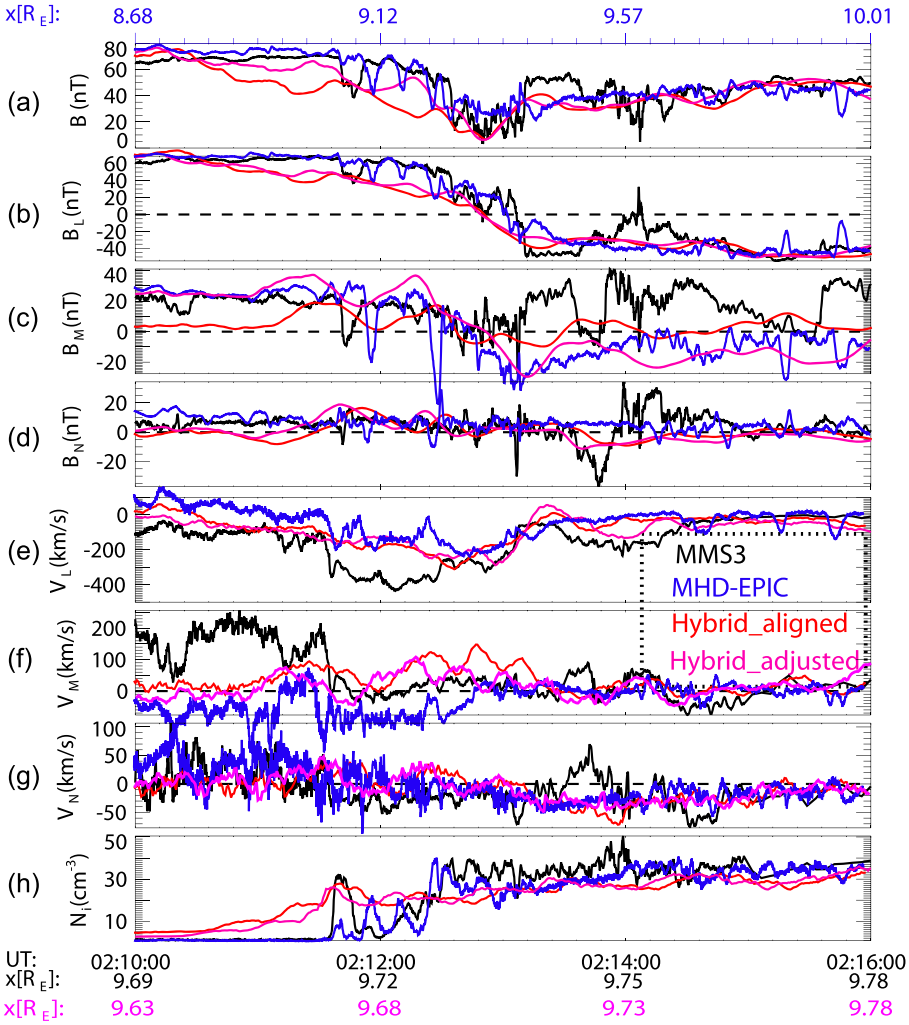

Figure 13. Plots of (a) B, magnetic field components (b) B_L, (c) B_M, (d) B_N, ion bulk flow components (e) V_L, (f) V_M, and (g) V_N, and (h) ion density N observed by MMS-3 (black) and obtained from the hybrid simulation (red) and the MHD_EMIC simulation (blue, from Chen et al., 2020) for the event of magnetopause crossing from 02:10 to 02:16 UT on 18 November 2015.

$z = -0.3\ R_E$. The simulated and observed V_L (in Figure 13e) and V_N (in Figure 13g) are generally similar, but with a time lag of about 36 s in the outflow V_L is seen in the simulation in Figure 13e. The MMS crossing exhibits a >400 km/s flow acceleration and a similar flow speed is also found in our simulated magnetopause boundary layer, but the exact location of it is slightly different from the observation. In addition, there is a normal electric field E_N pointing into the magnetopause current layer from either side of the magnetopause central current layer in both the simulation and the observation, indicating the ion diffusion region.

Typical ion velocity space properties associated with the ion jets in the magnetopause reconnection region obtained from our hybrid simulation and the MMS-3 observation are shown in Figure 14. Figure 14a depicts the contour plots of the magnetic field strength B in the noon meridian plane in a zoomed view obtained from the hybrid simulation, from $z = 8.0\ R_E$ to $12.0\ R_E$ and from $z = -5.0\ R_E$ to $5.0\ R_E$ at $t = 624.8$ s. The black lines superposed on the contours are along the local magnetic field directions projected onto the 2-D noon meridian plane. Figure 14b shows the 2-D cut of the 3-D ion distribution in the $v_{\parallel} - v_{\perp 1}$ plane at a chosen location centered at $(x, y, z) = (9.6, 0., 0.)\ R_E$ on the magnetosphere side of the current sheet in our simulation, marked by "C" in Figure 14a. Here, the ion parallel velocity component, $v_{\parallel}$, is along the local magnetic field direction, and the perpendicular component $v_{\perp 1}$ is perpendicular to the location magnetic

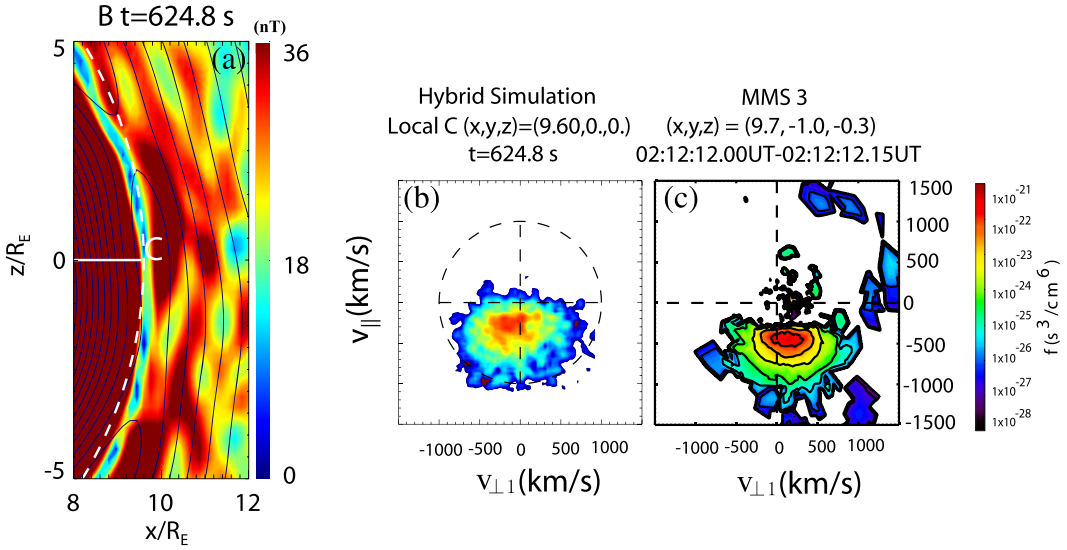

Figure 14. (a) Contour plots of B in the noon meridian plane, from $x = 8.0\ R_E$ to $12.0\ R_E$ and from $z = -5.0\ R_E$ to $5.0\ R_E$ obtained from the hybrid simulation at $t = 624.8$ s. Ion velocity distributions in the $v_{\|} - v_{\perp 1}$ plane obtained from (b) the hybrid simulation on the magnetosphere side of the current sheet, at the location marked by "C" in Figure 14a and (c) observed by MMS-3, where $v_{\|}$ is along the local magnetic field direction and $v_{\perp 1}$ is perpendicular to the location magnetic field along the $E \times B$ direction.

field along the $E \times B$ direction. The corresponding ion distribution in the $v_{\|} - v_{\perp 1}$ plane observed by MMS3 from 02:12:12.10 to 02:12:12.15 UT is shown in Figure 14c. In the observation from 02:12:12.10 to 02:12:12.15 UT, a strong magnetic field strength B (see Figure 13a), a positive B_L component (in Figure 13b), and a small ion density (in Figure 13h) are seen, which indicates that the MMS-3 spacecraft is situated on the magnetosphere side of the current sheet. A clear "D-shaped" distribution is observed by MMS-3, as seen in Figure 14c, when southward ion jets are detected from 02:12:12.10 to 02:12:12.15 UT by the spacecraft. The presence of the D-shaped ion distribution and the southward ion jets provides quantitative evidence for the occurrence of magnetic reconnection northward of the MMS-3 position in the magnetopause crossing (e.g., Fuselier et al., 1991). Similarly, a D-shaped ion distribution is found in the outflow region of the reconnection site in the hybrid simulation, as presented in Figure 14b, due to the time-of-flight effects of the transmitted magnetosheath plasma accelerated by reconnection. The "D" faces the direction of the accelerated ion jet, moving antiparallel to the ambient magnetic field, consistent with the MMS-3 spacecraft observation in Figure 14c as well as previous observations (Broll et al., 2017; Cowley, 1982; Fuselier et al., 1991) and hybrid simulations (e.g., Y. Lin & Lee, 1993a, 1993b; Tan et al., 2011). Again, the streaming direction is consistent with ions originating from the X line located northward of the location marked by "C" in Figure 14a.

For this magnetopause crossing event, the wave powers in the magnetosphere, magnetopause current sheet, and magnetosheath are an important aspect in our comparison with observation. The comparison of the wave powers is valuable to assess the performance of our numerical model and serves as a validation for further numerical simulations. Figure 15 shows the PSDs of the transverse ($\delta B_{\perp x}$ and $\delta B_{\perp y}$) and parallel ($\delta B_{\|}$) magnetic field fluctuations in the magnetosheath (left), magnetopause current sheet (middle), and magnetosphere (right) obtained from the MMS-3 observation and our hybrid simulation. The MMS-3 PSDs are averaged over 02:15–02:55 UT for the magnetosheath, over 02:10–02:15 UT for the current layer, and over 01:30–01:51 UT for the magnetosphere. Because of this time averaging, there is only a slight enhancement in $\delta B_{\|}$ at ~0.07 Hz in the magnetosheath corresponding to observed mirror mode waves, but still consistent with the hybrid simulation results in Figure 15. In general, the wave powers in the simulation agree well with observations in the magnetosheath and the current sheet. There is a −2.8 spectral index between 0.2 and 1.0 Hz in both the observation and the simulation, in the magnetosheath and the magnetopause current layer in Figure 15. For frequencies higher than 1 Hz, the PSD slope in our simulation becomes flatter. Compared with the observations, the PSD of hybrid simulation appears to be shifted

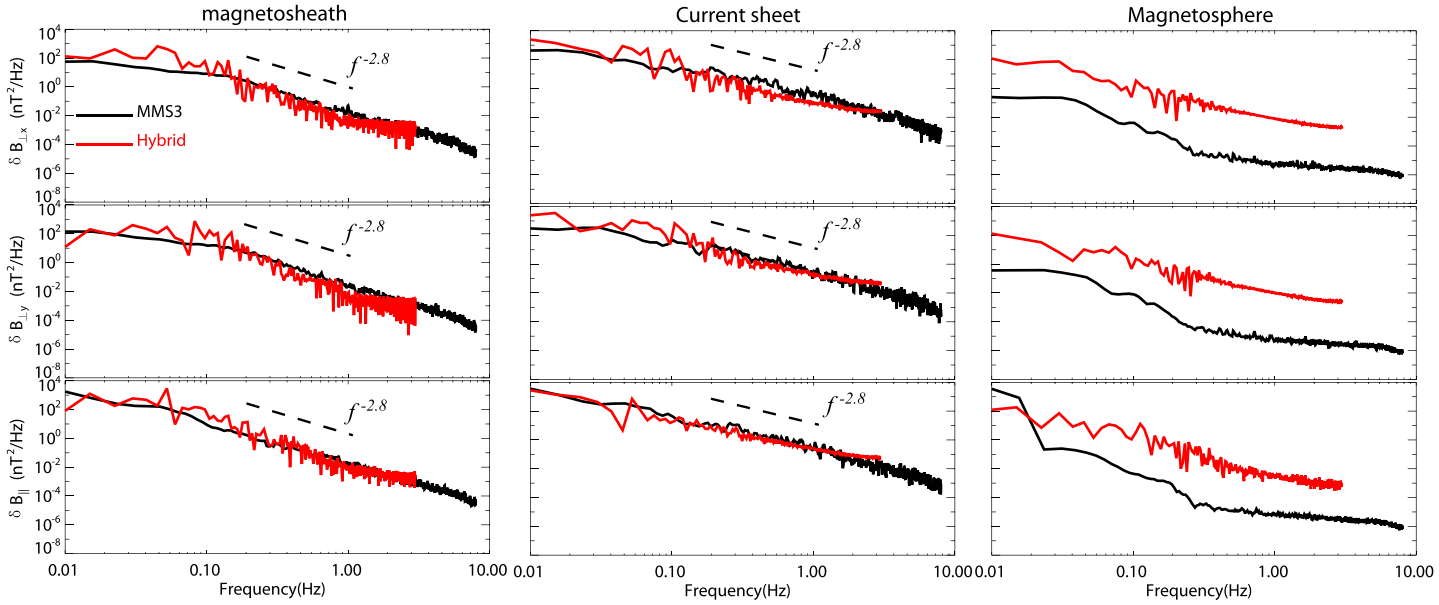

Figure 15. Magnetic field power spectral densities (PSDs) in the magnetosheath (left), magnetopause current sheet (middle), and magnetosphere (right), observed by MMS-3 (black) and obtained from the hybrid simulation (red).

slightly to the lower frequency side. This may be due to the time scaling used in the plotting. As described earlier, our scaling is based on a factor related to the faster global convection timescale used in the simulation. In Figure 15, we have scaled down the frequency by a factor 8.2, assuming that the timescales of the dynamics are related to the convection time. Some kinetic physics in the magnetopause current layer and in the magnetosheath, however, may be associated with the local ion gyrofrequency rather than the global convection. Since the solar wind ion gyrofrequency used in the simulation is realistic, no scaling would be necessary in that case. As a consequence, we may have overscaled the frequency toward the low frequencies. Overall, the hybrid model has well captured the electromagnetic wave powers on the ion scales, noting $\Omega_i \sim 4$ Hz. Nevertheless, an inconsistency between the simulation and observation is seen in the PSDs taken in the magnetosphere. This inconsistency may be due to the fact that the magnetospheric region in this simulation contains only the dayside part, which corresponds to a reduced inertia of the geomagnetic field. As a result, the effects of the solar wind on magnetospheric perturbations may be enlarged.

4. Summary and Discussion

In this study, we have presented results of a 3-D global hybrid simulation to investigate the structure of magnetopause reconnection and the effects of a tailward tilted geomagnetic dipole on magnetopause reconnection under a southward IMF. The simulation is carried out for the MMS magnetopause observation event on 18 November 2015 (Kitamura et al., 2016), and the simulation results are compared with the observation. Our key results are summarized as the follows.

1. The hybrid simulation shows that in the presence of a large geomagnetic dipole tilt (−27°) under the southward IMF, the subsolar reconnection X line (or site) in the dayside magnetopause shifts toward the Northern Hemisphere (at $z \approx 1.9\ R_E$). The simulation result is consistent with that observed by MMS and Geotail spacecraft (Kitamura et al., 2016), as well as previous observations and empirical predictions of the location of reconnection line (H. Hasegawa et al., 2010; Trattner et al., 2007).
2. The hybrid simulation shows that over the dayside global magnetopause, the reconnection regions are distributed in three areas: around middle latitudes in the northern dawn region, near the subsolar region, and around low latitudes near the equator in the dusk region. The near subsolar X lines are tilted and located north of the equator. Flux ropes/FTEs are generated over the magnetopause due to MXR. Around the subsolar region, the formation of multiple X lines begins from the generation of an X line above the equator. As the X line moves poleward, a new X line re-forms near the original location, and

the process repeats in time. This is consistent with the conclusions of Hasegawa et al. (2010) for subsolar reconnection sites during times of large dipole tilt, which shows flux ropes forms between the two X lines and move tailward. Dayside reconnection is found to be not in a steady state even though solar wind parameters are kept constant. The overall global structure of the magnetopause X lines, however, is nearly unchanged.

3. The ion diffusion region in the vicinity of the simulated X lines, a Hall electric field, and an asymmetric quadrupole Hall magnetic field signature are present. An ion density enhancement and ion heating are present inside the simulated flux ropes.
4. A single D-shaped ion distribution, associated with the transmitted and accelerated ion jets, is obtained in the simulated outflow region of reconnection.
5. By placing a virtual satellite in the simulation at the MMS orbit location, the simulated magnetopause crossing is compared with the MMS crossing. The structure of the dominant B_L component of magnetic field (and the field strength B) and the presence of the V_L component flow jet and the D-shaped ion velocity distribution are consistent with the MMS observations in the magnetopause crossing. In addition, the PSDs of magnetic field in the simulation, in general, agree well with that observed by MMS-3 spacecraft. Overall, the detailed structures at a specific location and/or time in the simulation are not exactly the same as the observation, but the overall structure and dynamics of the magnetopause reconnection are consistent with the observation.
6. By examining the magnetosheath waves for this event, it is found in our simulation that the ratio $P_{\perp}/P_{\parallel}$ stays above or near the marginal stability condition of the mirror mode wave in the middle region of the magnetosheath. Mirror mode waves with antiphase oscillations between B and N are present in the magnetosheath.

The above hybrid model-observation data comparison indicates that our 3-D hybrid simulation can capture the ion kinetic physics in the global magnetopause reconnection, while the global dynamics driven self-consistently by the solar wind. Previously, using MHD simulations, Raeder (2006) showed that FTEs only develop by multiple X line reconnection for a large dipole tilt during strong southward IMF, whereas there is a single X line steady reconnection at the dayside magnetopause in the case without a dipole tilt. However, Dorelli and Bhattacharjee (2009) reported in resistive MHD simulations that FTEs are generated during southward IMF with or without ta dipole tilt angle. Our simulation shows that under a tailward dipole tilt, near the subsolar region, flux ropes are formed between two X lines above the equatorial plane, which subsequently move poleward along the magnetopause boundary layer. Our simulation finds that neighboring reconnection sites and X lines could modify the local plasma conditions at the magnetopause, which further influences the reconnection rate. Both the magnetosheath flows and the outflow structures associated with the multiple reconnection sites may play important roles in the motion of the X lines. In addition, waves on the magnetosheath side of the reconnection current sheet may also have effects on the local reconnection rate and the motion of the magnetopause X lines. It is found in our simulation that the magnetopause reconnection is neither spatially nor temporally in a steady state even though solar wind parameters are kept constant.

In order to save the computation resources, the solar wind ion skin depth (and thus the ion Larmor radius) in unit of R_E used in our simulation is larger than that in reality by a factor of 8.2, and so is the ratio between the ion gyro period Ω_{i0}^{-1} and the solar wind convection time. In this paper, when compared the simulation results with the MMS observation, the time is scaled up (thus frequency scaled down) by a factor of 8.2 considering the shorter convection time used, while Ω_i in the simulation is realistic. For some local physics associated with the particle scales Ω_i, however, no scaling would be necessary. Therefore, the scaling factor applied in the paper may be somewhat an over correction. The scaling issue may contribute to the uncertainty in the frequency domain power spectra as well as in the detailed magnetopause structures observed by a virtual satellite shown in section 3.2. Comparison of the simulation results with observations provides a necessary and effective tool of validating the simulation results.

Data Availability Statement

The numerical data used for generating the presented figures are available via figshare (https://doi.org/10.6084/m9.figshare.11569311.v1). The MMS data sets are publicly available at the MMS Science Data Center (at https://lasp.colorado.edu/mms/sdc/public/). IDL routines for display of MMS data are also

publicly available in the current SPEDAS software package, which can be found through the SPEDAS website (http://spedas.org) and through the MMS Science Data Center (https://lasp.colorado.edu/mms/sdc/public/software/).

Acknowledgments
This work was supported by the Grants NASA-80NSSC17K0012 and NASA-NNX17AI47G and DoE Grant DEFOA-0001664 to Auburn University. The computer resources were provided by the National Supercomputer Center of China. The results in this paper are generated from our computer simulation code as described in section 22.

References

Angelopoulos, V., Cruce, P., Drozdov, A., Grimes, E. W., Hatzigeorgiu, N., King, D. A., et al. (2019). The Space Physics Environment Data Analysis System (SPEDAS). *Space Science Reviews*, *215*, 9. https://doi.org/10.1007/s11214-018-0576-4

Angelopoulos, V., McFadden, J. P., Larson, D., Carlson, C. W., Mende, S. B., Frey, H., et al. (2008). Tail reconnection triggering substorm onset. *Science*, *321*(5891), 931, Aug–935. https://doi.org/10.1126/science.1160495

Birn, J., Drake, J. F., Shay, M. A., Rogers, B. N., Denton, R. E., Hesse, M., et al. (2001). Geospace environment modeling (GEM) magnetic reconnection challenge. *Journal of Geophysical Research*, *106*(A3), 3715–3719. https://doi.org/10.1029/1999JA900449

Boardsen, S. A., Eastman, T. E., Sotirelis, T., & Green, J. L. (2000). An empirical model of the high-latitude magnetopause. *Journal of Geophysical Research*, *105*(A10), 23,193–23,219. https://doi.org/10.1029/1998JA000143

Broll, J. M., Fuselier, S. A., & Trattner, K. J. (2017). Locating dayside magnetopause reconnection with exhaust ion distributions. *Journal of Geophysical Research: Space Physics*, *122*, 5105–5113. https://doi.org/10.1002/2016JA023590

Burch, J. L., Moore, T. E., Torbert, R. B., & Giles, B. L. (2016). Magnetospheric Multiscale overview and science objectives. *Space Science Reviews*, *199*(1-4), 5–21. https://doi.org/10.1007/s11214-015-0164-9

Burch, J. L., & Phan, T. D. (2016). Magnetic reconnection at the dayside magnetosphere: Advances with MMS. *Geophysical Research Letters*, *43*, 8327–8338. https://doi.org/10.1002/2016GL069787

Cassak, P. A., & Fuselier, S. A. (2016). Reconnection at Earth's dayside magnetopause. In W. Gonzalez, & E. Parker (Eds.), *Magnetic reconnection: Concepts and applocations, asstrophysics and space science library* (Vol. 427, pp. 213–276). Hiedelberg, NY: Springer Cham. https://doi.org/10.1007/978-3-319-26432-5_6

Cassak, P. A., Genestreti, K. J., Burch, J. L., Phan, T. D., Shay, M. A., Swisdak, M., et al. (2017). The effect of a guide field on local energy conversion during asymmetric magnetic reconnection: Particle-in-cell simulation. *Journal of Geophysical Research: Space Physics*, *122*, 11,523–11,542. https://doi.org/10.1002/2017JA024555

Chen, Y., Toth, G., Hietala, H., Vines, S. K., Zou, Y., Nishimura, Y., et al. (2020). Magnetohydrodynamic with embedded particle-in-cell simulation of the Geospace Environment Modeling dayside kinetic processes challenge event, *Earth and Space Science*, *7*, e2020EA001331. https://doi.org/10.1029/2020EA001331

Cowley, S. W. H. (1982). The causes of convection in the Earth's magnetosphere: A review of developments during the IMS. *Reviews of Geophysics*, *20*(3), 531–565. https://doi.org/10.1029/RG020i003p00531

Crooker, N. U. (1979). Dayside merging and cusp geometry. *Journal of Geophysical Research*, *84*(A3), 951–959. https://doi.org/10.1029/JA084iA03p00951

Dorelli, J. C., & Bhattacharjee, A. (2009). On the generation and topology of flux transfer events. *Journal of Geophysical Research*, *114*, A06213. https://doi.org/10.1029/2008JA013410

Doss, C. E., Komar, C. M., Cassak, P. A., Wilder, F. D., Eriksson, S., & Drake, J. F. (2015). Asymmetric magnetic reconnection with a flow shear and applications to the magnetopause. *Journal of Geophysical Research: Space Physics*, *120*, 7748–7763. https://doi.org/10.1002/2015JA021489

Dungey, J. W. (1961). Interplanetary magnetic field and the auroral zones. *Physical Review Letters*, *6*(2), 47–48. https://doi.org/10.1103/PhysRevLett.6.47

Eastwood, J. P., Phan, T. D., Oieroset, M., Shay, M. A., Malakit, K., Swisdak, M., et al. (2013). Influence of asymmetries and guide fields on the magnetic reconnection diffusion region in collisionless space plasmas. *Plasma Physics and Controlled Fusion*, *55*, 124001. https://doi.org/10.1088/0741-3335/55/12/124001

Fu, Z. F., & Lee, L. C. (1985). Simulation of multiple X-line reconnection at the dayside magnetopause. *Geophysical Research Letters*, *12*(5), 291–294. https://doi.org/10.1029/GL012i005p00291

Fuselier, S. A., Klumpar, D. M., & Shelley, E. G. (1991). Ion reflection and transmission during reconnection at the Earth's subsolar magnetopause. *Geophysical Research Letters*, *18*(2), 139–142. https://doi.org/10.1029/90GL02676

Fuselier, S. A., Trattner, K. J., & Petrinec, S. M. (2011). Antiparallel and component reconnection at the dayside magnetopause. *Journal of Geophysical Research*, *116*, A10227. https://doi.org/10.1029/2011JA016888

Fuselier, S. A., Trattner, K. J., Petrinec, S. M., & Lavraud, B. (2012). Dayside magnetic topology at the Earth's magnetopause for northward IMF. *Journal of Geophysical Research*, *117*, A08235. https://doi.org/10.1029/2012JA017852

Génot, V., Budnik, E., Hellinger, P., Passot, T., Belmont, G., Trávní˘cek, P. M., et al. (2009). Mirror structures above and below the linear instability threshold: Cluster observations, fluid model and hybrid simulations. *Annales de Geophysique*, *27*(2), 601–615. https://doi.org/10.5194/angeo-27-601-2009

Glocer, A., Dorelli, J., Toth, G., Komar, C. M., & Cassak, P. A. (2016). Separator reconnection at the magnetopause for predominantly northward and southward IMF: Techniques and results. *Journal of Geophysical Research: Space Physics*, *121*, 140–156. https://doi.org/10.1002/2015JA021417

Gonzalez, W. D., & Mozer, F. S. (1974). A quantitative model for the potential resulting from reconnection with an arbitrary interplanetary magnetic field. *Journal of Geophysical Research*, *79*(28), 4186–4194. https://doi.org/10.1029/JA079i028p04186

Gosling, J. T., Skoug, R. M., McComas, D. J., & Smith, C. W. (2005). Direct evidence for magnetic reconnection in the solar wind near 1 AU. *Journal of Geophysical Research*, *110*, A01107. https://doi.org/10.1029/2004JA010809

Guo, Z., Lin, Y., Wang, X., & Du, A. (2018). Magnetosheath reconnection before magnetopause reconnection driven by interplanetary tangential discontinuity: A three-dimensional global hybrid simulation with the oblique interplanetary magnetic field. *Journal of Geophysical Research: Space Physics*, *123*, 9169–9186. https://doi.org/10.1029/2018JA025679

Hasegawa, A. (1969). Drift mirror instability of the magnetosphere. *Physics of Fluids*, *12*(12), 2642–2650. https://doi.org/10.1063/1.1692407

Hasegawa, H., Wang, J., Dunlop, M. W., Pu, Z. Y., Zhang, Q. H., Lavraud, B., et al. (2010). Evidence for a flux transfer event generated by multiple X-line reconnection at the magnetopause. *Geophysical Research Letters*, *37*, L16101. https://doi.org/10.1029/2010GL044219

Hoilijoki, S., Ganse, U., Pfau-Kempf, Y., Cassak, P. A., Walsh, B. M., Hietala, H., et al. (2017). Reconnection rates and X line motion at the magnetopause: Global 2D-3V hybrid-Vlasov simulation results. *Journal of Geophysical Research: Space Physics*, *122*, 2877–2888. https://doi.org/10.1002/2016JA023709

Hoilijoki, S., Souza, V. M., Walsh, B. M., Janhunen, P., & Palmroth, M. (2014). Magnetopause reconnection and energy conversion as influenced by the dipole tilt and the IMF Bx. *Journal of Geophysical Research: Space Physics*, *119*, 4484–4494. https://doi.org/10.1002/2013JA019693

Khotyaintsev, Y. V., Graham, D. B., Norgren, C., Eriksson, E., Li, W., Johlander, A., et al. (2016). Electron jet of asymmetric reconnection. *Geophysical Research Letters*, *43*, 5571–5580. https://doi.org/10.1002/2016GL069064

Kitamura, N., Hasegawa, H., Saito, Y., Shinohara, I., Yokota, S., Nagai, T., et al. (2016). Shift of the magnetopause reconnection line to the winter hemisphere under southward IMF conditions: Geotail and MMS observations. *Geophysical Research Letters*, *43*, 5581–5588. https://doi.org/10.1002/2016GL069095

Komar, C. M., Cassak, P. A., Dorelli, J. C., Glocer, A., & Kuznetsova, M. M. (2013). Tracing magnetic separators and their dependence on IMF clock angle in global magnetospheric simulations. *Journal of Geophysical Research: Space Physics*, *118*, 4998–5007. https://doi.org/10.1002/jgra.50479

Lin, J., & Forbes, T. G. (2000). Effects of reconnection on the coronal mass ejection process. *Journal of Geophysical Research*, *105*(A2), 2375–2392. https://doi.org/10.1029/1999JA900477

Lin, R. L., Zhang, X. X., Liu, S. Q., Wang, Y. L., & Gong, J. C. (2010). A three-dimensional asymmetric magnetopause model. *Journal of Geophysical Research*, *115*, A04207. https://doi.org/10.1029/2009JA014235

Lin, Y., Johnson, J. R., & Wang, X. Y. (2010). Hybrid simulation of mode conversion at the magnetopause. *Journal of Geophysical Research*, *115*, A04208. https://doi.org/10.1029/2009JA014524

Lin, Y., & Lee, L. C. (1993a). Structure of the dayside reconnection layer in resistive MHD and hybrid models. *Journal of Geophysical Research*, *98*(A3), 3919–3934. https://doi.org/10.1029/92JA02363

Lin, Y., & Lee, L. (1993b). Structure of reconnection layers in the magnetosphere. *Space Science Reviews*, *65*, 59–179.

Lin, Y., & Lee, L. C. (1995). Simulation study of the Riemann problem associated with the magnetotail reconnection. *Journal of Geophysical Research*, *100*(A10), 19,227–19,237. https://doi.org/10.1029/95JA01549

Lin, Y., & Wang, X. Y. (2005). Three-dimensional global hybrid simulation of dayside dynamics associated with the quasi-parallel bow shock. *Journal of Geophysical Research*, *110*, A12216. https://doi.org/10.1029/2005JA011243

Lin, Y., Wang, X. Y., Lu, S., Perez, J. D., & Lu, Q. (2014). Investigation of storm time magnetotail and ion injection using three-dimensional global hybrid simulation. *Journal of Geophysical Research: Space Physics*, *119*, 7413–7432. https://doi.org/10.1002/2014JA020005

Lin, Y., & Xie, H. (1997). Formation of reconnection layer at the dayside magnetopause. *Geophysical Research Letters*, *24*(24), 3145–3148. https://doi.org/10.1029/97GL03278

Liu, Y.-H., Hesse, M., & Kuznetsova, M. (2015). Orientation of X lines in asymmetric magnetic reconnection—Mass ratio dependency. *Journal of Geophysical Research: Space Physics*, *120*, 7331–7341. https://doi.org/10.1002/2015JA021324

Liu, Y.-H., Hesse, M., Li, T. C., Kuznetsova, M., & Le, A. (2018). Orientation and stability of asymmetric magnetic reconnection X line. *Journal of Geophysical Research: Space Physics*, *123*, 4908–4920. https://doi.org/10.1029/2018JA025410

Liu, Z. Q., Lu, J. Y., Kabin, K., Yang, Y. F., Zhao, M. X., & Cao, X. (2012). Dipole tilt control of the magnetopause for southward IMF from global magnetohydrodynamic simulations. *Journal of Geophysical Research*, *117*, A07207. https://doi.org/10.1029/2011JA017441

Lu, J. Y., Liu, Z. Q., Kabin, K., Jing, H., Zhao, M. X., & Wang, Y. (2013). The IMF dependence of the magnetopause from global MHD simulations. *Journal of Geophysical Research: Space Physics*, *118*, 3113–3125. https://doi.org/10.1002/jgra.50324

Luhmann, J. G., Walker, R. J., Russell, C. T., Crooker, N. U., Spreiter, J. R., & Stahara, S. S. (1984). Patterns of potential magnetic field merging sites on the dayside magnetopause. *Journal of Geophysical Research*, *89*(A3), 1739–1742. https://doi.org/10.1029/JA089iA03p01739

Masuda, S., Kosugi, T., Hara, H., Tsuneta, S., & Ogawara, Y. (1994). A loop-top hard X-ray source in a compact solar flare as evidence for magnetic reconnection. *Nature*, *371*(6497), 495–497. https://doi.org/10.1038/371495a0

Moore, T. E., Fok, M.-C., & Chandler, M. O. (2002). The dayside reconnection X line. *Journal of Geophysical Research*, *107*(A10), 1332. https://doi.org/10.1029/2002JA009381

Nagai, T., Shinohara, I., Fujimoto, M., Hoshino, M., Saito, Y., Machida, S., & Mukai, T. (2001). Geotail observations of the hall current system: Evidence of magnetic reconnection in the magnetotail. *Journal of Geophysical Research*, *106*, 25,929–25,949. https://doi.org/10.1029/2001JA900038

Nakamura, R., Baumjohann, W., Asano, Y., Runov, A., Balogh, A., Owen, C. J., et al. (2006). Dynamics of thin current sheets associated with magnetotail reconnection. *Journal of Geophysical Research*, *111*, A11206. https://doi.org/10.1029/2006JA011706

Øieroset, M., Phan, T. D., Fujimoto, M., Lin, R. P., & Lepping, R. P. (2001). In situ detection of collisionless reconnection in the Earth's magnetotail. *Nature*, *412*(6845), 414–417. https://doi.org/10.1038/35086520

Onsager, T. G., Scudder, J. D., Lockwood, M., & Russell, C. T. (2001). Reconnection at the high-latitude magnetopause during northward interplanetary magnetic field conditions. *Journal of Geophysical Research*, *106*(A11), 25,467–25,488. https://doi.org/10.1029/2000JA000444

Pang, Y., Lin, Y., Deng, X. H., Wang, X. Y., & Tan, B. (2010). Three-dimensional hybrid simulation of magnetosheath reconnection under northward and southward interplanetary magnetic field. *Journal of Geophysical Research*, *115*, A03203. https://doi.org/10.1029/2009JA014415

Park, K. S., Ogino, T., & Walker, R. J. (2006). On the importance of antiparallel reconnection when the dipole tilt and IMF B_y are nonzero. *Journal of Geophysical Research*, *111*, A05202. https://doi.org/10.1029/2004JA010972

Phan, T., et al. (2018). Electron magnetic reconnection without ion coupling in Earth's turbulent magnetosheath. *Nature*, *557*(7704), 202–206. https://doi.org/10.1038/s41586-018-0091-5

Phan, T. D., Paschmann, G., Twitty, C., Mozer, F. S., Gosling, J. T., Eastwood, J. P., et al. (2007). Evidence for magnetic reconnection initiated in the magnetosheath. *Geophysical Research Letters*, *34*, L14104. https://doi.org/10.1029/2007GL030343

Pollock, C., Moore, T., Jacques, A., Burch, J., Gliese, U., Saito, Y., et al. (2016). Fast Plasma Investigation for Magnetospheric Multiscale. *Space Science Reviews*, *199*(1-4), 331–406. https://doi.org/10.1007/s11214-016-0245-4

Pritchett, P. L. (2001). Geospace environment modeling magnetic reconnection challenge: Simulations with a full particle electromagnetic code. *Journal of Geophysical Research*, *106*(A3), 3783–3798. https://doi.org/10.1029/1999JA001006

Raeder, J. (2006). Flux transfer events: 1. Generation mechanism for strong southward IMF. *Annales de Geophysique*, *24*(1), 381–392. https://doi.org/10.5194/angeo-24-381-2006

Retinò, A., Sundkvist, D., Vaivads, A., Mozer, F., André, M., & Owen, C. J. (2007). In situ evidence of magnetic reconnection in turbulent plasma. *Nature Physics*, *3*(4), 235–238. https://doi.org/10.1038/nphys574

Retinò, A., Vaivads, A., & Bale, S. D. (2007). Dissipation in turbulent plasma due to reconnection in thin current sheets. *Physical Review Letters*, *99*, 025004. https://doi.org/10.1103/PhysRevLett.99.025004

Russell, C. T., Anderson, B. J., Baumjohann, W., Bromund, K. R., Dearborn, D., Fischer, D., et al. (2016). The Magnetospheric Multiscale magnetometers. *Space Science Reviews*, *199*(1-4), 189–256. https://doi.org/10.1007/s11214-014-0057-3

Russell, C. T., Wang, Y. L., & Raeder, J. (2003). Possible dipole tilt dependence of dayside magnetopause reconnection. *Geophysical Research Letters*, *30*(18), 1937. https://doi.org/10.1029/2003GL017725

Shay, M. A., Phan, T. D., Haggerty, C. C., Fujimoto, M., Drake, J. F., Malakit, K., et al. (2016). Kinetic signatures of the region surrounding the X-line in asymmetric (magnetopause) reconnection. *Geophysical Research Letters*, *43*, 4145–4154. https://doi.org/10.1002/2016GL069034

Sibeck, D. G., & Omidi, N. (2012). Flux transfer events: Motion and signatures. *Journal of Atmospheric and Solar-Terrestrial Physics*, *87-88*, 20–24. https://doi.org/10.1016/j.jastp.2011.07.010

Sonnerup, B. U. Ö. (1974). Magnetopause reconnection rate. *Journal of Geophysical Research*, *79*(10), 1546–1549. https://doi.org/10.1029/JA079i010p01546

Sonnerup, B. U. Ö., & Scheible, M. (1998). Minimum and maximum variance analysis. In G. Paschmann, & P. W. Daly (Eds.), *Analysis methods for multi-spacecraft data*, *ISSI Scientific Report Series SR-001* (pp. 185–220). Noordwijk, Netherlands: ESA Publ.

Soucek, J., Lucek, E., & Dandouras, I. (2008). Properties of magnetosheath mirror modes observed by Cluster and their response to changes in plasma parameters. *Journal of Geophysical Research*, *113*, A04203. https://doi.org/10.1029/2007JA012649

Sun, T. R., Tang, B. B., Wang, C., Guo, X. C., & Wang, Y. (2019). Large-scale characteristics of flux transfer events on the dayside magnetopause. *Journal of Geophysical Research: Space Physics*, *124*, 2425–2434. https://doi.org/10.1029/2018JA026395

Swift, D. W. (1996). Use of a hybrid code for global-scale plasma simulation. *Journal of Computational Physics*, *126*(1), 109–121. https://doi.org/10.1006/jcph.1996.0124

Tan, B., Lin, Y., Perez, J. D., & Wang, X. Y. (2011). Global-scale hybrid simulation of dayside magnetic reconnection under southward IMF: Structure and evolution of reconnection. *Journal of Geophysical Research*, *116*, A02206. https://doi.org/10.1029/2010JA015580

Tan, B., Lin, Y., Perez, J. D., & Wang, X. Y. (2012). Global-scale hybrid simulation of cusp precipitating ions associated with magnetopause reconnection under southward IMF. *Journal of Geophysical Research*, *117*, A03217. https://doi.org/10.1029/2011JA016871

Terasawa, T. (1983). Hall current effect on tearing mode instability. *Geophysical Research Letters*, *10*(6), 475–478. https://doi.org/10.1029/GL010i006p00475

Trattner, K. J., Burch, J. L., Cassak, P. A., Ergun, R., Eriksson, S., Fuselier, S. A., et al. (2018). The transition between antiparallel and component magnetic reconnection at Earth's dayside magnetopause. *Journal of Geophysical Research: Space Physics*, *123*, 10,177–10,188. https://doi.org/10.1029/2018JA026081

Trattner, K. J., Fuselier, S. A., & Petrinec, S. M. (2004). Location of the reconnection line for northward interplanetary magnetic field. *Journal of Geophysical Research*, *109*, A03219. https://doi.org/10.1029/2003JA009975

Trattner, K. J., Mulcock, J. S., Petrinec, S. M., & Fuselier, S. A. (2007). Location of the reconnection line at the magnetopause during southward IMF conditions. *Geophysical Research Letters*, *34*, L03108. https://doi.org/10.1029/2006GL028397

Trattner, K. J., Petrinec, S. M., Fuselier, S. A., & Phan, T. D. (2012). The location of the reconnection line: Testing the maximum magnetic shear model with THEMIS observations. *Journal of Geophysical Research*, *117*, A01201. https://doi.org/10.1029/2011JA016959

Vasyliunas, V. M. (1975). Theoretical models of magnetic merging. *Reviews of Geophysics*, *13*(1), 303–336. https://doi.org/10.1029/RG013i001p00303

Wang, H., Lin, Y., Wang, X., & Guo, Z. (2019). Generation of kinetic Alfvén waves in dayside magnetopause reconnection: A 3-D global-scale hybrid simulation. *Physics of Plasmas*, *26*, 072102. https://doi.org/10.1063/1.5092561

Wang, R., Lu, Q., Nakamura, R., Huang, C., Du, A., Guo, F., et al. (2016). Coalescence of magnetic flux ropes in the ion diffusion region of magnetic reconnection. *Nature Physics*, *12*(3), 263–267. https://doi.org/10.1038/nphys3578

Webster, J. M., Burch, J. L., Reiff, P. H., Daou, A. G., Genestreti, K. J., Graham, D. B., et al. (2018). Magnetospheric Multiscale dayside reconnection electron diffusion region events. *Journal of Geophysical Research: Space Physics*, *123*, 4858-4878. https://doi.org/10.1029/2018JA025245

Xie, H., & Lin, Y. (2000). Two-dimensional hybrid simulation of the dayside reconnection layer and associated ion transport. *Journal of Geophysical Research*, *105*(A11), 25,171–25,183. https://doi.org/10.1029/2000JA000143

Yordanova, E., Vörös, Z., Varsani, A., Graham, D. B., Norgren, C., Khotyaintsev, Y. V., et al. (2016). Electron scale structures and magnetic reconnection signatures in the turbulent magnetosheath. *Geophysical Research Letters*, *43*, 5969–5978. https://doi.org/10.1002/2016GL069191

Young, D. T., Burch, J. L., Gomez, R. G., Los Santos, A., Miller, G. P., Wilson, P. IV, et al. (2016). Hot plasma composition Analyzer for the Magnetospheric Multiscale mission. *Space Science Reviews*, *199*(1-4), 407–470. https://doi.org/10.1007/s11214-014-0119-6